Centro Euro-Mediterraneo
per i Cambiamenti Climatici

Research Papers
Issue RP0110
September 2011

SERC - Climate SERvices

EXTREME EVENTS IN HIGH RESOLUTION CMCC REGIONAL AND GLOBAL CLIMATE MODELS

By **Enrico Scoccimarro**
INGV, CMCC
scoccimarro@bo.ingv.it

and **Silvio Gualdi**
INGV, CMCC
gualdi@bo.ing.it

and **Antonella Sanna**
CMCC
antonella.sanna@cmcc.it

and **Edoardo Bucchignani**
CIRA, CMCC
e.bucchignani@cira.it

and **Myriam Montesarchio**
CMCC
m.montesarchio@cira.it

SUMMARY Within the framework of the FUME EU project a set of climate projections covering the period 1970-2100 has been performed using a global General Circulation model (CMCC-Med) and a Regional Climate model (CMCC-CLM). Simulation outputs have been post-processed in order to investigate extreme events based on three principal weather parameters: precipitation, surface temperature and 10 metre wind. Using these parameters, several indexes for extreme event characterizations have been computed on daily time basis over 4 seasons. Trends and variability have been computed and examined both for the global and regional model.

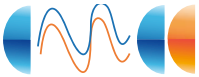

CMCC Research Papers

02

Centro Euro-Mediterraneo per i Cambiamenti Climatici

Contents

1 Introduction

One of the conclusions of the IPCC Fourth Assessment Report (AR4, Solomon 2007 [12]) is that there are evidences that climate change affects the frequency, intensity, and length of many extreme events, such as floods, droughts, storms and extreme temperatures. At the same time, changes in ecosystems and natural resources further increase the consequences of extreme weather events. Extreme events are hard to study and even harder to predict because they are, by definition, rare and obey different statistical laws than averages (Naveau et al., 2005 [8]).

The availability of climate simulations data covering the period 1970-2100 from a global Coupled General Circulation Model (CGCM) and a high resolution Regional Climate model (RCM) provided by the CMCC give the possibility to investigate weather/climatic extreme events over the Euro-Mediterranean Region in terms of spatial and temporal evolution. The characteristics of the two climate models involved in this study and the simulation performed are described in Section 2. In Section 3 we define indexes of extreme events that can be involved in determining fire development conditions, using the climate models simulation outputs at daily time scale. Section 4 gives a brief description of the results obtained at global scale, taking into account only part of the computed indexes and periods described in section 3. In section 5 we illustrate and discuss the results obtained from a dynamical downscaling with a high resolution atmospheric model for the Mediterranean region.

2 Climate models and simulations used in this analysis

One of the objectives of the FUME project is the definition of a series of indexes of extreme climatic conditions favourable for wild fires development and propagation, and the assessment of how these indexes might possibly change as a consequence of climate change. To this aim CMCC implemented global and regional climate simulations covering the period 1970-2100. The global simulations are performed using the CMCC-MED CGCM whereas the regional ones are produced using the CMCC-CLM RCM. In the next subsections the two models are described together with the simulation settings used.

2.1 The CMCC-MED global simulations

The model employed at global scale is the CMCC-MED (Gualdi et al. 2011 [6], Scoccimarro et al. 2011 [11]) coupled atmosphere-ocean general circulation model. CMCC-MED is an evolution of the INGV-SXG (Gualdi et al. 2008 [7], Bellucci et al. 2008 [2]) and the ECHAM-OPA-LIM (Fogli et al. 2009 [5], Vichi et al. 2011 [14]) models. The model has a focus on the Mediterranean region and a very high resolution model of the Mediterranean Sea has been included as a component of the coupled atmosphere-ocean system in order to improve the representation of the dynamical processes that characterize this region. Specifically the global ocean component is simulated with a coarse-resolution global ocean model, whereas a high-resolution eddy-permitting model is used for the Mediterranean Sea (Oddo et al. 2009 [9]).

The global ocean component has horizontal resolution of 2^o x 2^o with a meridional refinement near the equator, approaching a minimum 0.5^o grid spacing. The Mediterranean Sea has a horizontal resolution of $1/16^o$ and 71 levels along the vertical.

The atmospheric model component is

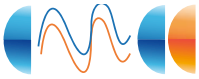

ECHAM5 (Roeckner et al. 2003 [4]) in its T159 configuration, corresponding to a horizontal resolution of about 0.75^o x 0.75^o. In the vertical, the atmospheric model has 31 hybrid sigma-pressure levels and top at 10 hPa.

Every 160 minutes (coupling frequency), heat, mass and momentum fluxes are computed and provided to the ocean model by the atmospheric model. Sea Surface Temperature (SST) and sea surface velocities are provided to the atmospheric model by both the global and the Mediterranean ocean models.

The CMCC-MED model has been implemented with the aim to perform climate scenario experiments. Here we present results from a climate simulation covering the 1950-2100 period, following the IPCC 20C3M protocol for the 20^{th} Century and the A1B scenario for the 21^{st} Century (http://www-pcmdi.llnl.gov/ipcc/about_ipcc.php). The simulation starts from an equilibrium state obtained by integrating the model for 200 years with greenhouse gasses (GHGs) concentrations corresponding to 1950s conditions.

2.2 The CMCC-CLM regional simulations

CMCC-CLM (Rockel, 2008 [10]) is the climate version of the regional COSMO model (Steppeler, 2003 [13]), which is the operational non-hydrostatic mesoscale weather forecast model developed by the German Weather Service. Successively, the model has been updated by the CLM-Community, in order to develop also climatic applications. In the CMCC-CLM version implemented over the Euro-Mediterranean region, the horizontal resolution is 0.12^o (14 km), thus the complex physiography of the region is represented better. The non-hydrostatic modelling allows providing a good description of the convective phenomena, which are generated by vertical movement (through transport and turbulent mixing) of the properties of the fluid as energy (heat), water vapour and momentum. Convection can redistribute significant amounts of moisture, heat and mass on small temporal and spatial scales. Furthermore convection can cause severe precipitation events (as thunderstorm or cluster of thunderstorms).

3 Indexes for extreme events characterization

The proposed investigation method focuses on the three principal weather fields involved in fire danger conditions development, such as surface temperature, precipitation and wind velocity. For each of them the computation of several indicators (subsections 3.1, 3.2, 3.3) has been done on daily time basis over 4 seasons defined as December-February (DJF), March-May (MAM), June-August (JJA), September-November (SON). These indicators characterize each model grid point over the relative spatial model domain (global/regional). The computed indexes are provided in netCDF format. To mark the regions affected by trends in extreme events occurrence in the period 1970-2100, we define trend maps considering only grid points where the detected trend results statistically significant (verified at 90% level with a bootstrap method). These trend maps are defined over five periods of 30 years: 1971-2000 1981-2010, 2011-2040, 2041-2070, 2071-2100, and two periods of 65 years: 1971-2035 and 2036-2100 In summary, with this deliverable we provide:

- 60 (30 indexes X 2 domains: global and Mediterranean) indexes time series as netcdf files: each file contains 4 time series (130 years) corresponding to the four seasons defined above. The Mediterranean domain is defined has the region

between 2^{o}W and 38^{o}E in longitude and between 30^{o}N and 50^{o}N in latitude.

- 420 (30 indexes X 2 domains X 7 periods) trend patterns as netcdf files: each file contains 4 maps corresponding to the four seasons.
- 1680 (30 indexes X 2 domains X 7 periods X 4 seasons) trend maps as .png figures.

In sections 4 and 5, only few of them will be described.

3.1 Temperature

Extreme temperature events are mainly associated to persistent large scale synoptic patterns, producing anomalous advection or regional persistence of air masses. Particularly relevant for the Mediterranean environment is the frequency and duration of heat waves and the increase of highest temperature values (Carril et al., 2008 [3]). Extremely high temperature events must be investigated through indexes computed using daily maximum temperature, but also extremely low temperature events must be considered, using the daily minimum temperature, in order to detect periods and regions less prone to fire development in terms of temperature.

3.1.1 Indicators

We define the following indicators based on temperature:

- 5^{th} Percentile of the daily minimum temperature: TN5P
- 10^{th} Percentile of the daily minimum temperature: TN10P
- 95^{th} Percentile of the daily minimum temperature: TN95P
- 90^{th} Percentile of the daily minimum temperature: TN90P
- Seasonal average of minimum daily temperature: MEANTN
- 5^{th} Percentile of the daily maximum temperature: TX5P
- 10^{th} Percentile of the daily maximum temperature: TX10P
- 95^{th} Percentile of the daily maximum temperature: TX95P
- 90^{th} Percentile of the daily maximum temperature: TX90P
- Seasonal average of maximum daily temperature: MEANTX
- Total number of consecutive (only series $>=$ 6 days) days with maximum daily temperature exceeding the long term (1971-2100) 90^{th} percentile: WSDI90
- Total number of consecutive (only series $>=$ 6 days) days with minimum daily temperature is below the long term (1971-2100) 10^{th} percentile: CSDI10

3.2 Precipitation

Source of precipitation are mainly large synoptic systems but, especially during summer, strong convective storms might play a fundamental role in inhibiting fire development over the Mediterranean region. In order to detect periods and regions more prone to fire development as a consequence of drought conditions, together with the percentile indexes the maximum number of consecutive dry days must be considered (CDD, 3.2.2).

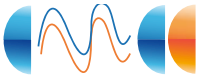

3.2.1 Indicators

We define the following indexes based on total precipitation:

- 95^{th} Percentile of the total daily precipitation: PREC95P
- 90^{th} Percentile of the total daily precipitation: PREC90P
- 5^{th} Percentile of the total daily precipitation: PREC5P
- 10^{th} Percentile of the total daily precipitation: PREC10P
- Number of days with daily precipitation exceeding the long term (1971-2100) 90^{th} percentile : R90N
- Number of days with daily precipitation exceeding the long term (1971-2100) 95^{th} percentile : R95N
- Number of days with daily precipitation lower than the long term (1971-2100) 10^{th} percentile : RL10N
- Number of days with daily precipitation lower than the long term (1971-2100) 5^{th} percentile : RL5N
- Averaged daily precipitation over wet days (wet day defined if precipitation is $>=$ 1[mm/day]): SDII
- Maximum (not total) number of consecutive dry days (dry day defined if precipitation is $<$ 1 [mm/day]): CDD

3.3 Winds

To support the analysis of wind induced drying effect on fuels, percentile indexes computed over the 10 meter daily wind speed are proposed. It is also well known that the rate of spread of a wildfire increases markedly when a wind springs up (Beer, 1990 [1]), suggesting that bursts indicators might be useful. To explore the bursts effect, In addition to the daily mean wind speed indexes, we propose to compute percentile indexes using the maximum wind speed (module) reached over the saving period. This field is provided by both CMCC-MED and CMCC-CLM climate models.

3.3.1 Indicators

We define the following indexes based on wind velocity:

- 95^{th} Percentile of the 10 meter wind speed: WI95P
- 90^{th} Percentile of the 10 meter wind speed: WI90P
- Number of days with daily wind speed exceeding the long term (1971-2100) 90^{th} percentile : WI90N
- Number of days with daily wind speed exceeding the long term (1971-2100) 95^{th} percentile : WI95N
- 95^{th} Percentile of the 10 meter maximum wind speed: WIMAX95P
- 90^{th} Percentile of the 10 meter maximum wind speed: WIMAX90P
- Number of days with maximum wind speed exceeding the long term (1971-2100) 90^{th} percentile : WIMAX90N
- Number of days with maximum wind speed exceeding the long term (1971-2100) 95^{th} percentile : WIMAX95N

4 Extreme events at global scale

In order to provide a short description of the computed indexes, in this paragraph winter (december-january-february, DJF) and summer (june-july-august, JJA) results are shown.

4.1 Temperature

The seasonal average of minimum daily temperature (MEANTN), averaged over the first 30 years of simulation (1971-2000) is shown in the upper panel of figure 1 (MEANTN, DJF) and figure 2 (MEANTN, JJA). These two figures show also the trend computed over 1971-2035 (hereafter DT1) and 2036-2100 (hereafter DT2) periods: DT1 trend is shown in the middle panel and DT2 in the bottom panel. Over the Arctic region a positive trend in both DT1 and DT2 periods is found, reaching 4^{o}C/decade in DT2 over the Barents sea during Boreal winter (Figure 1). During the Boreal summer a positive pattern is evident over the Antarctic Ocean (Figure 2). These positive patterns in MEANTN trends lead to sea-ice melting over the mentioned region during the scenario evolution and are confirmed by 10^{th} percentile of the daily minimum temperature (TN10P) that shows similar trend patterns but more pronounced (Figure 3 and 4). Similar features associated with the sea-ice are evident also in the Bering Sea and Greenland Sea during DJF. Also the maximum daily temperature (MEANTX, figure 5 and 6) and the 90^{th} percentile of the daily maximum temperature (TX90P, figure 7 and 8) show trends very similar to what has been found for the minimum daily temperature.

The total number of consecutive days with maximum daily temperature exceeding the long term (1971-2100) 90^{th} percentile (WSDI90) is an important index to highlight the tendency to have hot periods. Figure 9 (WSDI90, DJF) and figure 10 (WSDI90, JJA) show that large portion of the globe are interested by a large positive trend during the period DT2. In DT1 the trend is much weaker. The positive trend from 2036 onward has its maximum over the tropical oceans (8 days/decade), especially in the central equatorial Pacific Ocean, West Atlantic Ocean and Indian Ocean. However large trends in WSDI90 are found in central Africa, northern part of South America and Saudi Arabia with values as large as 4 days/decade in DT2 (figure 9 and 10). To investigate the tendency in the occurrence of extreme cold periods, the CSDI10 index (total number of consecutive days with minimum daily temperature below the long term 10^{th} percentile) is plot in figure 11 (CSDI10, DJF) and 12 (CSDI10, JJA). During the DT1 period a negative trend interests the tropical belt indicating that the number of consecutive cold days is reduced up to 2036. The trend appears to be much weaker in the period DT2 indicating a stabilization of this index in the second part of the XXI century.

4.2 Precipitation

The extreme events of low precipitation can be identified looking at the 10^{th} percentile of the total daily precipitation (PREC10P). Figure 13 (PREC10P, DJF) and figure 14 (PREC10P, JJA) show in the top panel the PREC10P averaged over the first simulated 30 years (1971:2000). In the DT2 period, PREC10P exhibits strong positive organized patterns in equatorial west Pacific Ocean, south of the equator during DJF (Figure 13, bottom panel) and in equatorial east Pacific Ocean and Indian Ocean, north of the equator, during JJA (Figure 14, bottom panel). In both seasons a less pronounced but significant positive pattern is shown in the Antarctic circumpolar region. PREC10P negative patterns (indicating the tendency to driest extreme dry events) are evident in DT2 over sub-regions

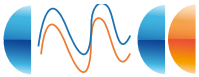

of Brazil in both seasons. Concerning the extreme high precipitation events, the PREC90P index (Figure 15 and 16) shows a positive trend in DT2, more extended in JJA, in the equatorial pacific and a negative trend in the eastern Indian ocean during JJA, indicating less extreme precipitation events tendency near Sumatra, in this season.

Figure 17 and 18 show the maximum number (not total) of consecutive dry days (defined as days in which precipitation $<=$ 1 mm/day) respectively in DJF and JJA (CDD). Focusing on the land regions to highlight potential drought conditions, the area most interested by positive trends in CDD is the eastern Europe and western Asia between 35^{o}N and 50^{o}N during JJA during the period DT2.

4.3 Winds

The 90th percentile of wind speed at 10 meter (WI90P index) averaged over 1971-2000 shows maximum values in the winter season (Boreal hemisphere - DJF, figure 19, top panel; austral hemisphere - JJA, figure 21, top panel). Positive trend in WI90P index indicates potential increase of extreme events in terms of surface winds. As figure 19 and figure 21 show, the model simulation indicates a clear tendency to a decrease of extreme events of surface winds over most of the globe, both in winter and summer. However some weak tendency to increased wind extreme events is visible in the Arctic region and in the Southern Ocean in Boreal and austral winter respectively. The trends in WI90N (number of days with daily wind speed exceeding the long term 90th percentile) are shown in figure 20 and figure 22 for northern winter and northern summer respectively. The patterns of WI90N trend confirm the model tendency to a reduction of extreme events in surface winds, especially over the ocean. Interestingly, over some areas of Africa and South America WI90N shows positive trends in the period DT2 (figure 20 and 22, bottom panels). The tendencies found in 10 meter daily averaged wind indexes are confirmed by percentiles computed using gusts (WIMAX90P and WIMAX90N), as shown in Figures 23, 24, 25 and 26.

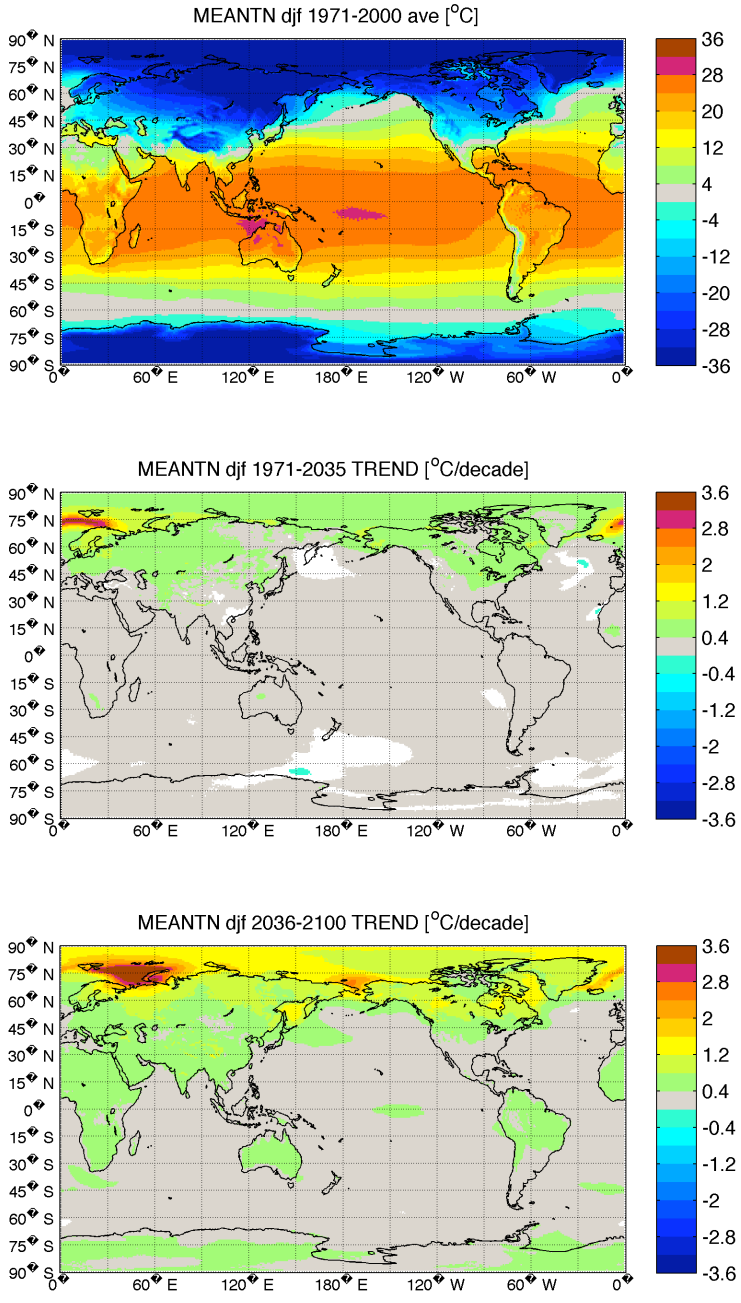

Figure 1:
MEANTN index computed for DJF season: seasonal average of daily minimum temperature. The first panel shows the average of this index over the 1971-2000 considered period. The last two panes show the index linear trend during 1971-2035 and 2036-2100. White patterns identify grid points where the computed trend is not statistically significant.

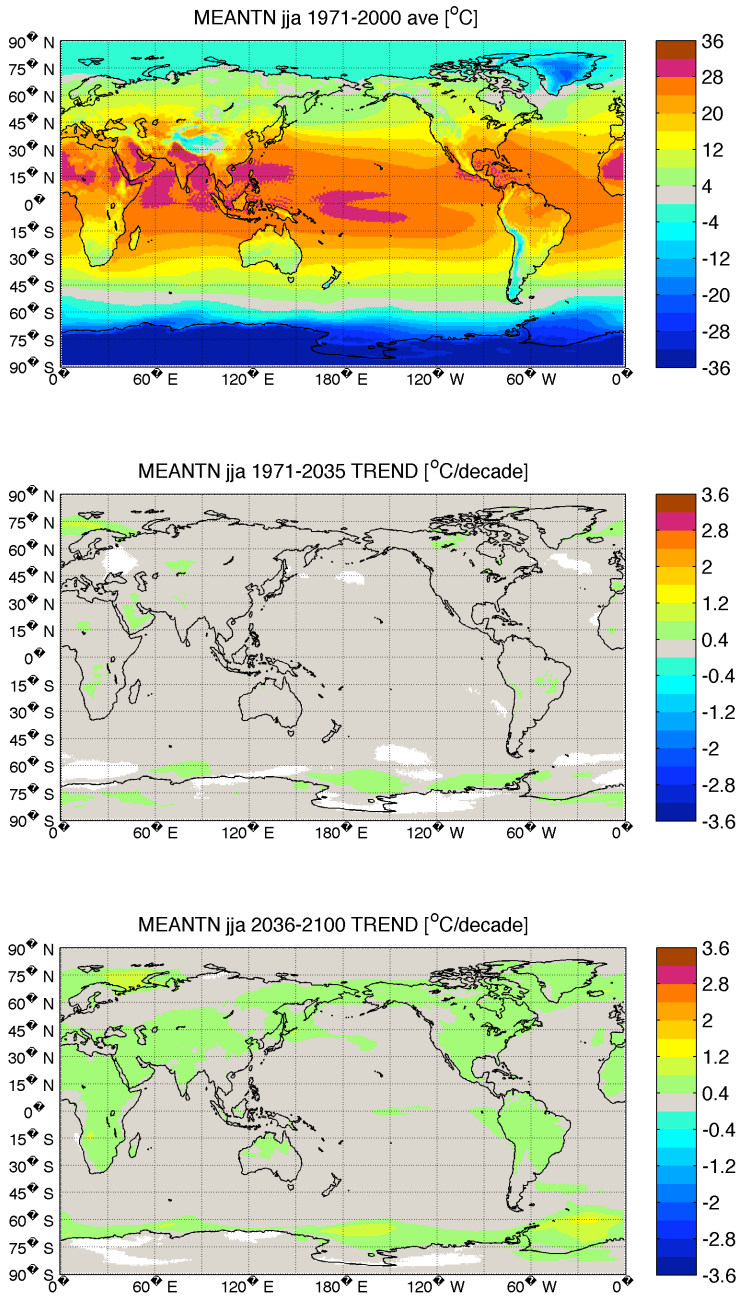

Figure 2:
MEANTN index computed for JJA season: seasonal average of daily minimum temperature. The first panel shows the average of this index over the 1971-2000 considered period. The last two panes show the index linear trend during 1971-2035 and 2036-2100. White patterns identify grid points where the computed trend is not statistically significant.

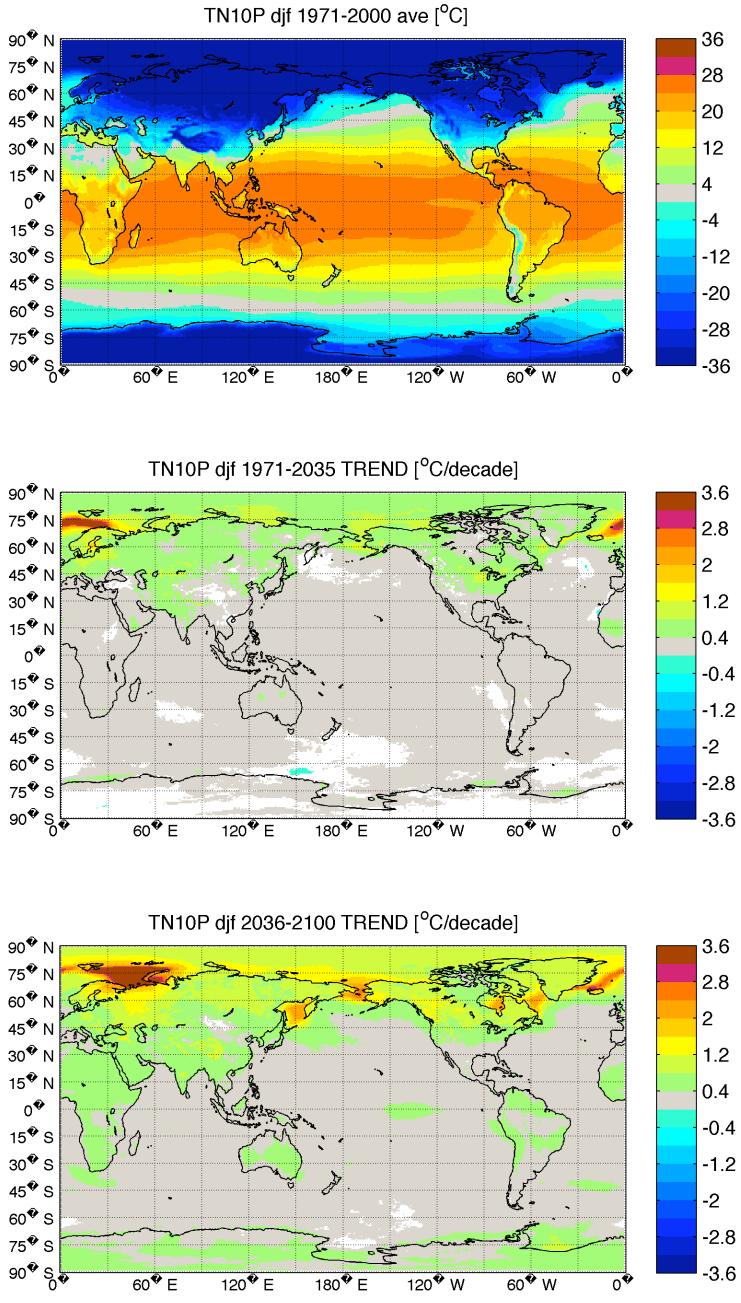

Figure 3:
TN10P index computed for DJF season: 10^{th} percentile of the daily minimum temperature. The first panel shows the average of this index over the 1971-2000 considered period. The last two panes show the index linear trend during 1971-2035 and 2036-2100. White patterns identify grid points where the computed trend is not statistically significant.

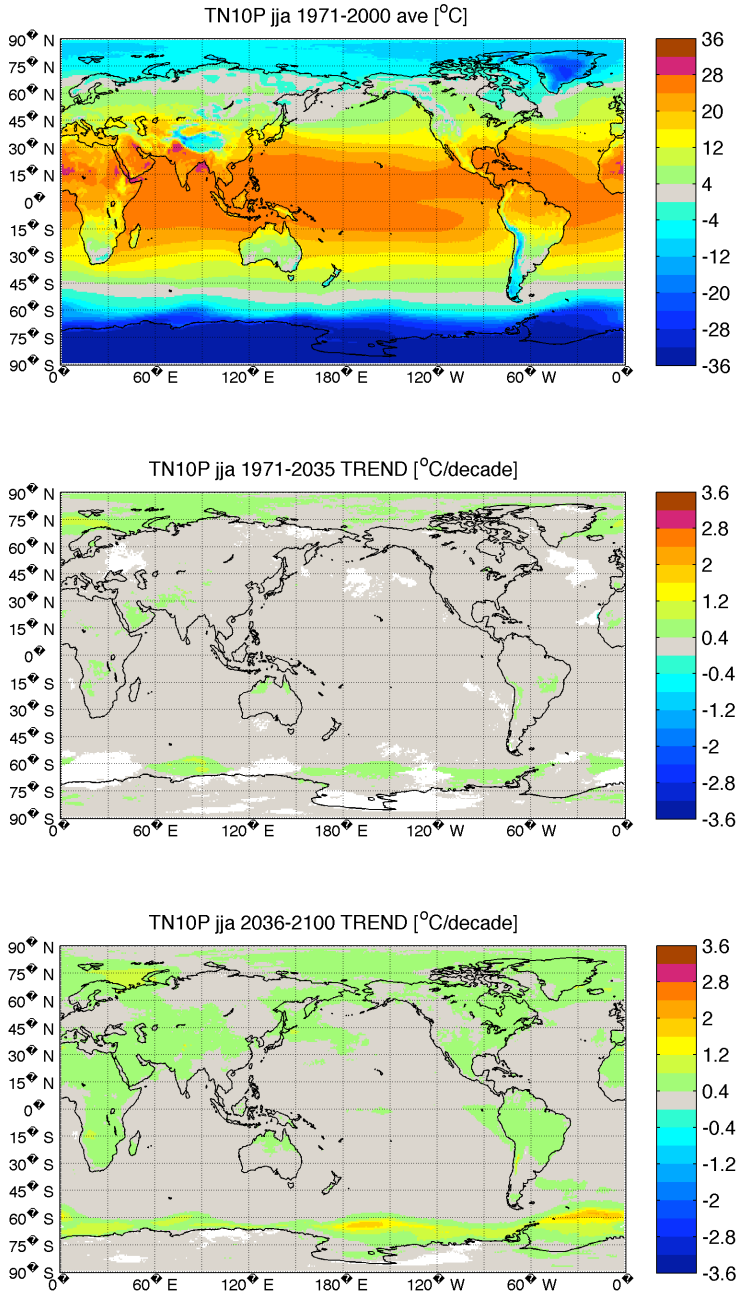

Figure 4:
TN10P index computed for JJA season: 10^{th} percentile of the daily minimum temperature. The first panel shows the average of this index over the 1971-2000 considered period. The last two panes show the index linear trend during 1971-2035 and 2036-2100. White patterns identify grid points where the computed trend is not statistically significant.

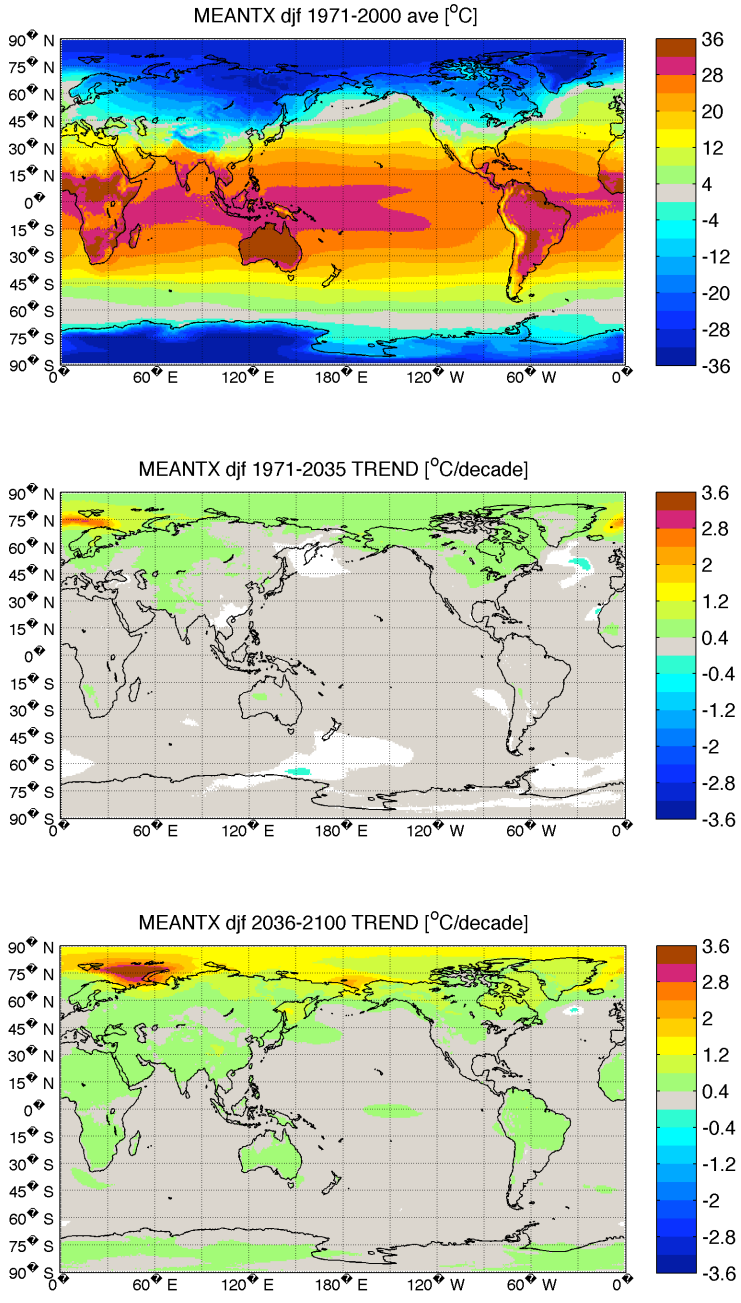

Figure 5:
MEANTX index computed for DJF season: seasonal average of daily maximum temperature. The first panel shows the average of this index over the 1971-2000 considered period. The last two panes show the index linear trend during 1971-2035 and 2036-2100. White patterns identify grid points where the computed trend is not statistically significant.

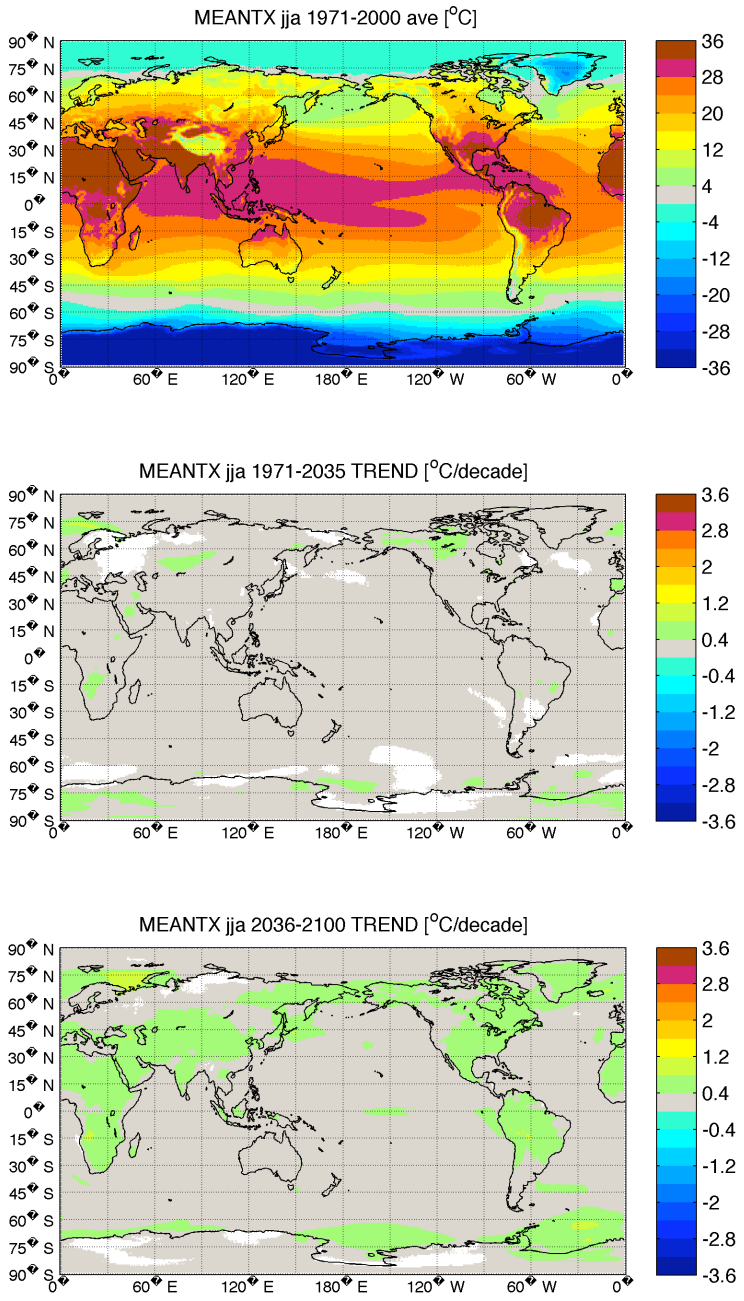

Figure 6:
MEANTX index computed for JJA season: seasonal average of daily maximum temperature. The first panel shows the average of this index over the 1971-2000 considered period. The last two panes show the index linear trend during 1971-2035 and 2036-2100. White patterns identify grid points where the computed trend is not statistically significant.

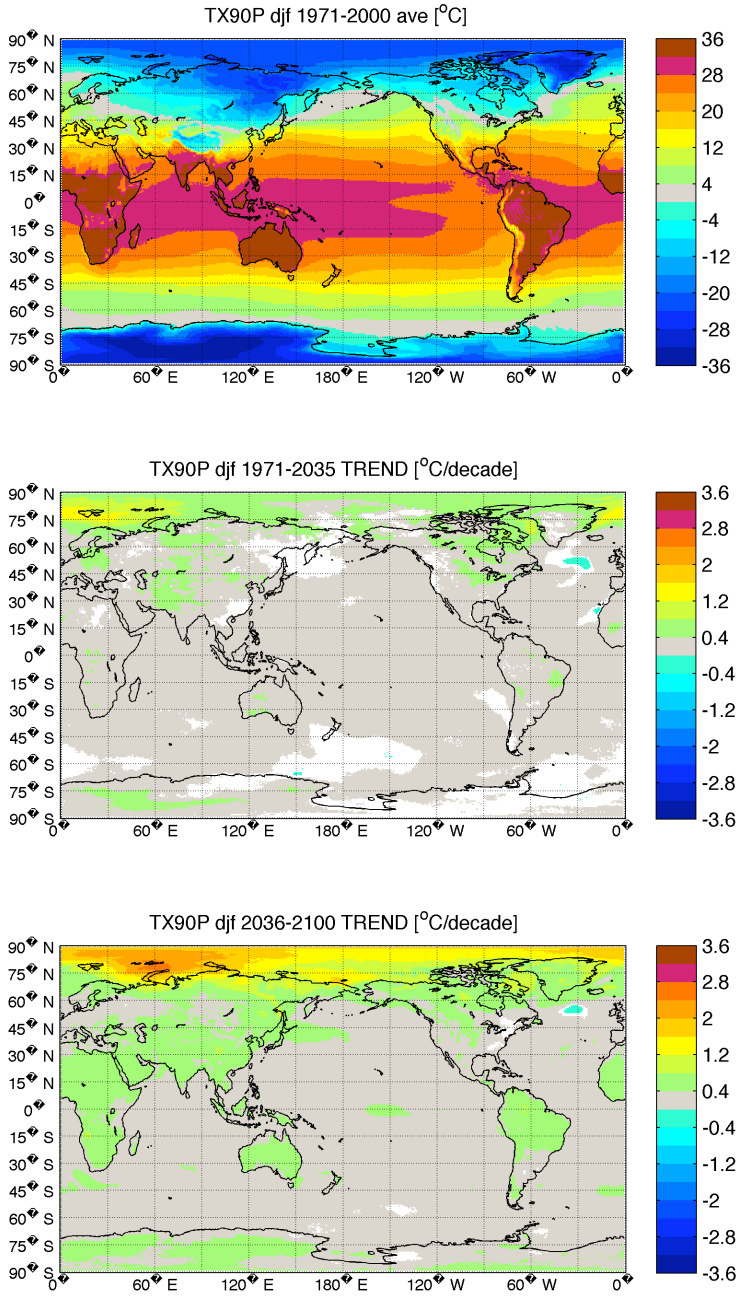

Figure 7:
TX90P index computed for DJF season: 90^{th} percentile of the daily maximum temperature. The first panel shows the average of this index over the 1971-2000 considered period. The last two panes show the index linear trend during 1971-2035 and 2036-2100. White patterns identify grid points where the computed trend is not statistically significant.

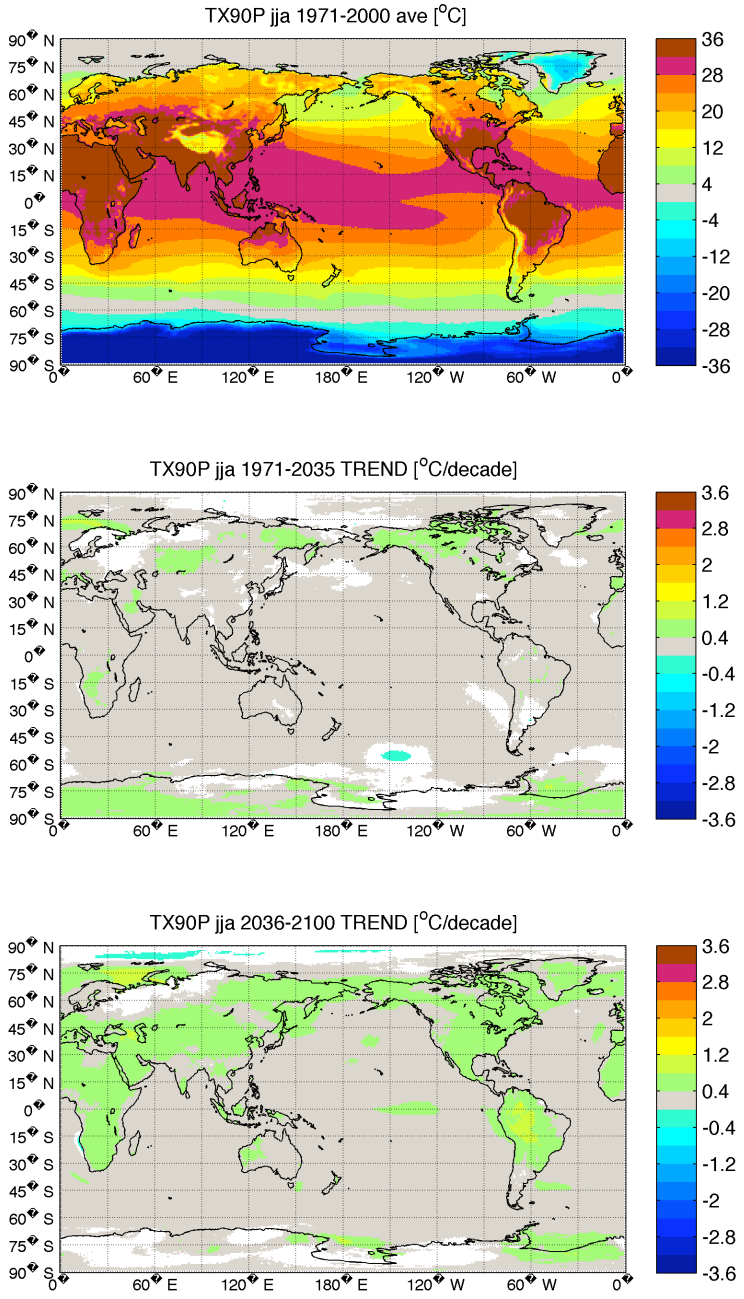

Figure 8:
TX90P index computed for JJA season: 90^{th} percentile of the daily maximum temperature. The first panel shows the average of this index over the 1971-2000 considered period. The last two panes show the index linear trend during 1971-2035 and 2036-2100. White patterns identify grid points where the computed trend is not statistically significant.

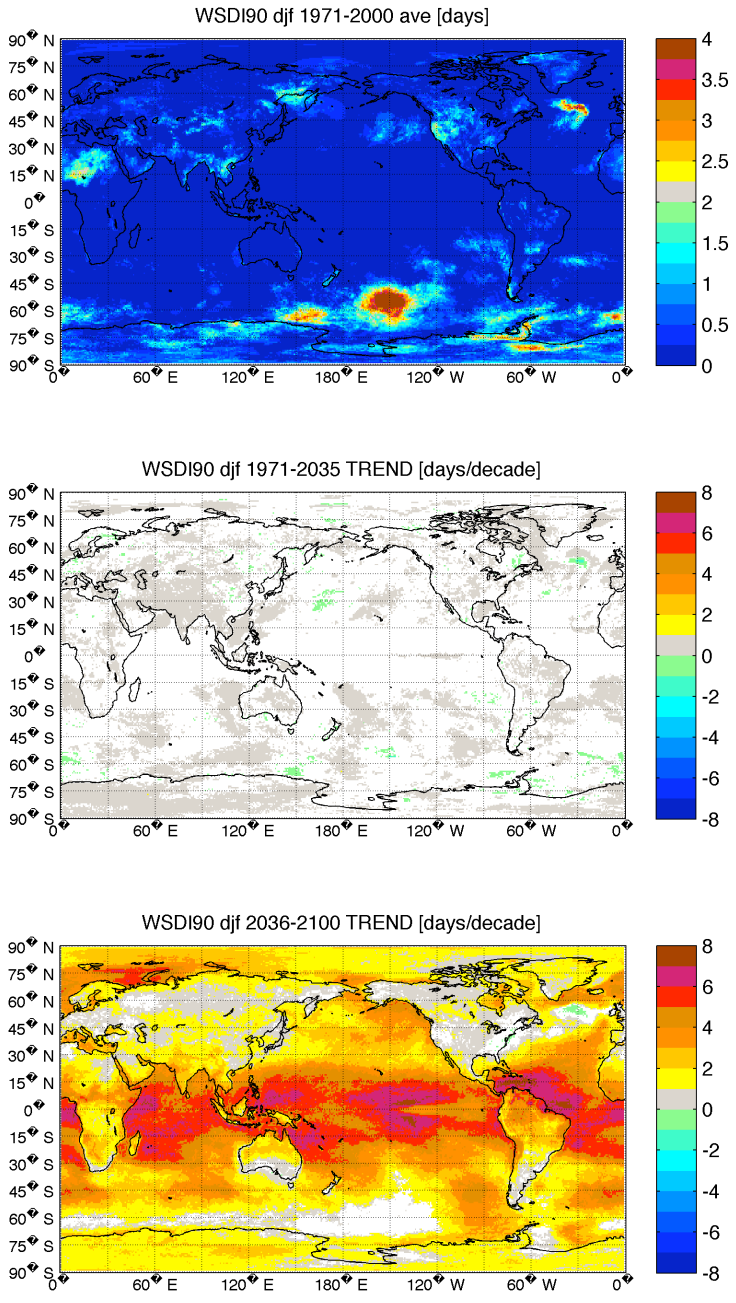

Figure 9:
WSDI90 index computed for DJF season: total number of consecutive days with maximum daily temperature exceeding the long term (1971-2100) 90^{th} percentile. The first panel shows the average of this index over the 1971-2000 considered period. The last two panes show the index linear trend during 1971-2035 and 2036-2100.

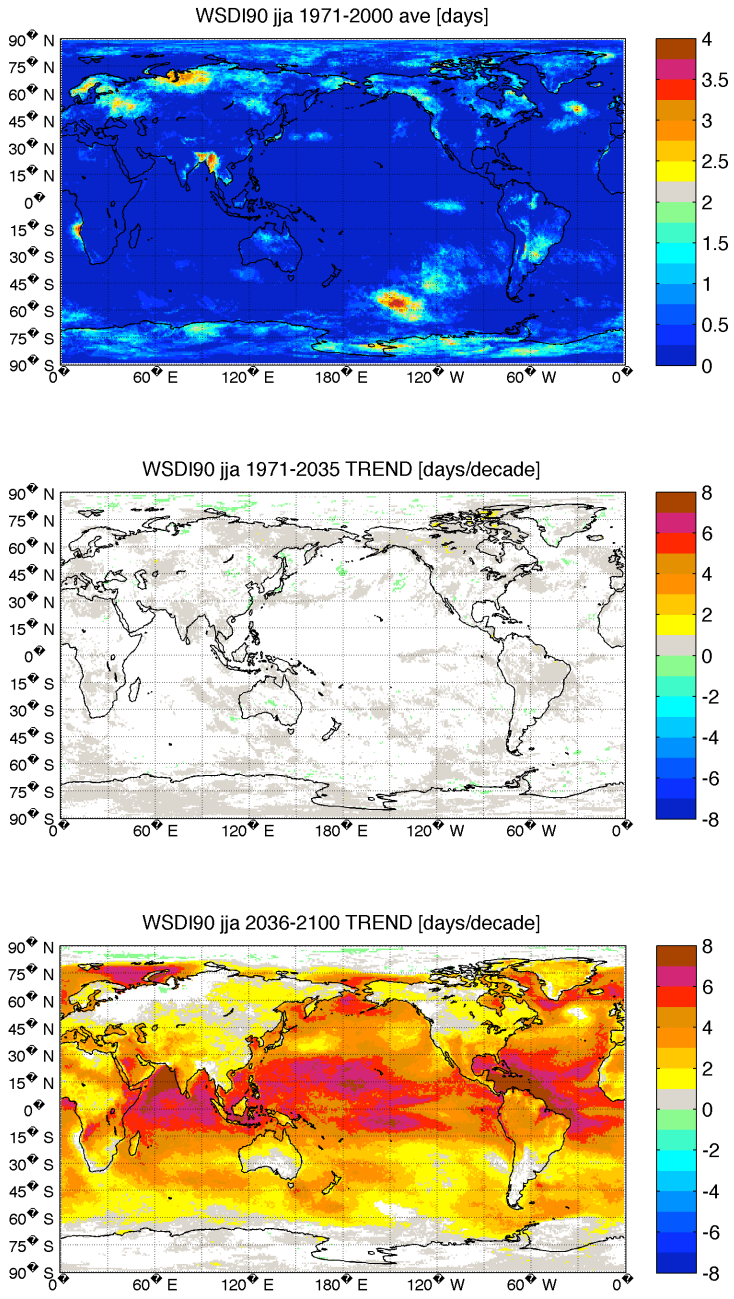

Figure 10:
WSDI90 index computed for JJA season: total number of consecutive days with maximum daily temperature exceeding the long term (1971-2100) 90^{th} percentile. The first panel shows the average of this index over the 1971-2000 considered period. The last two panes show the index linear trend during 1971-2035 and 2036-2100.

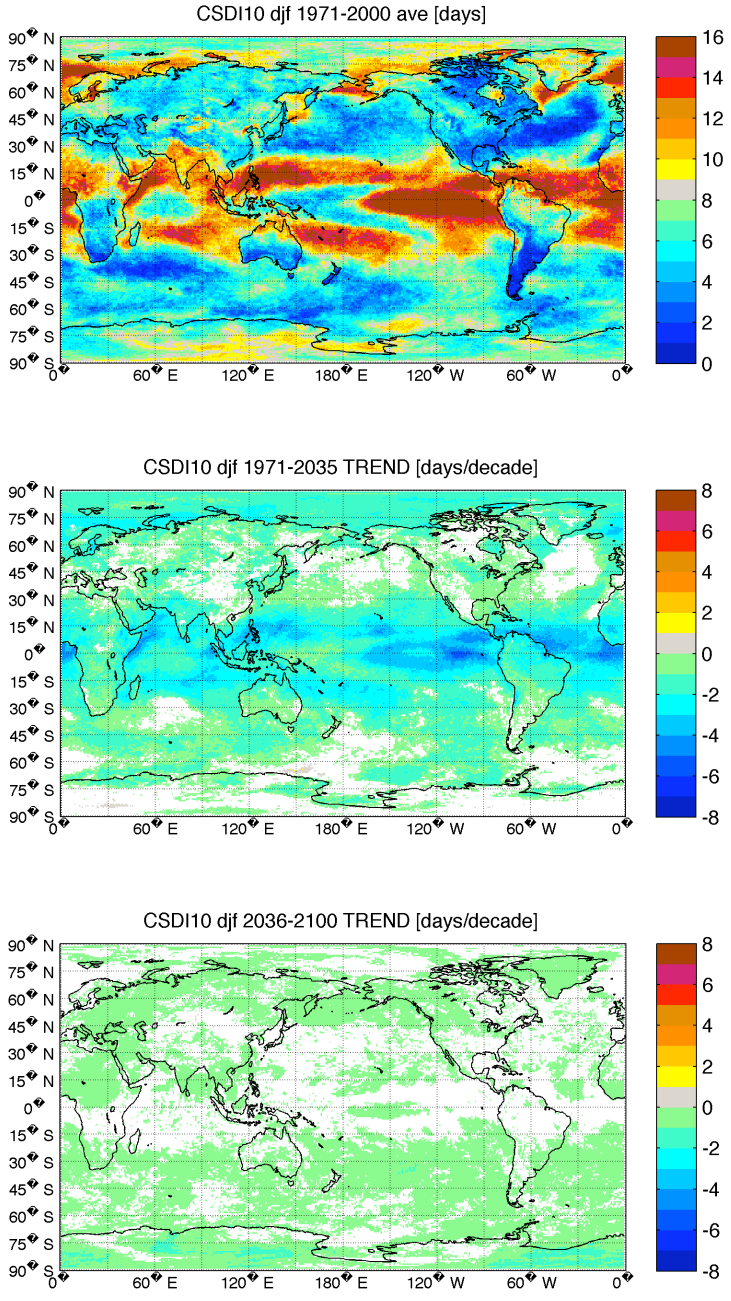

Figure 11:
CSDI10 index computed for DJF season: total number of consecutive days with minimum daily temperature below the long term (1971-2100) 10^{th} percentile. The first panel shows the average of this index over the 1971-2000 considered period. The last two panes show the index linear trend during 1971-2035 and 2036-2100.

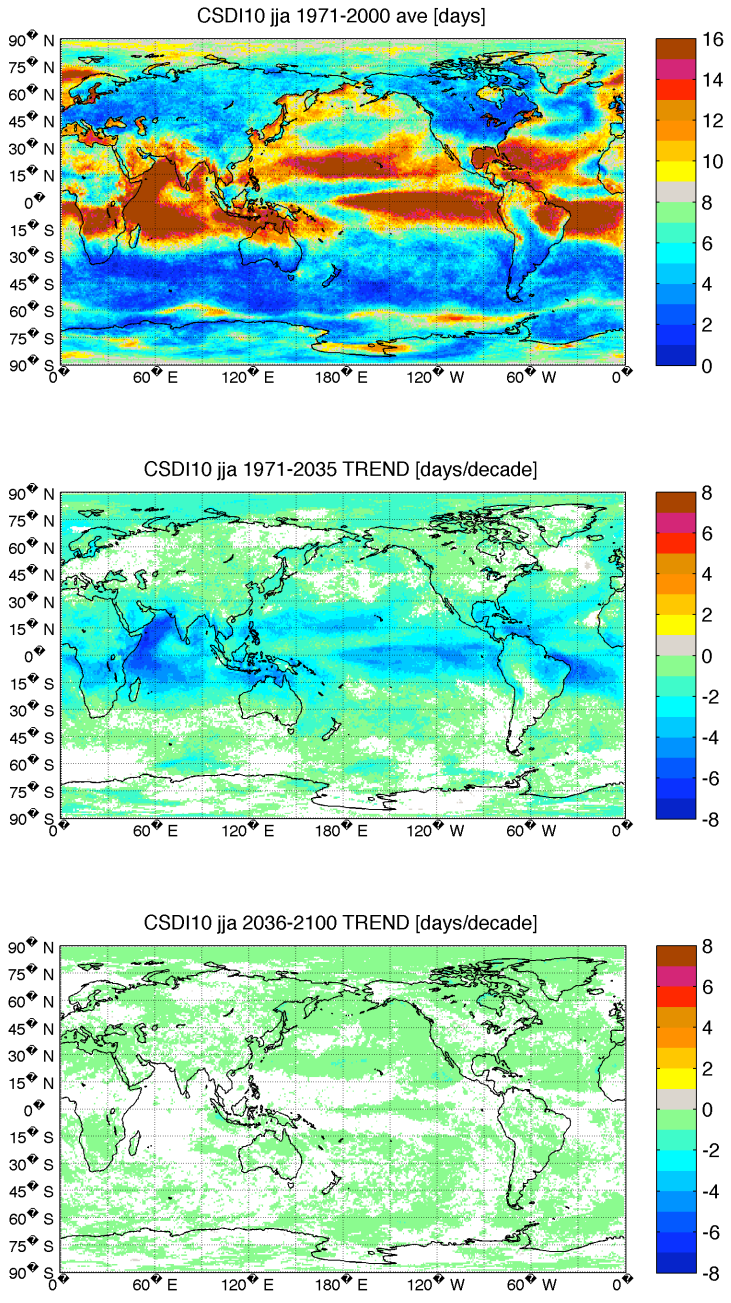

Figure 12:
CSDI10 index computed for JJA season: total number of consecutive days with minimum daily temperature below the long term (1971-2100) 10^{th} percentile. The first panel shows the average of this index over the 1971-2000 considered period. The last two panes show the index linear trend during 1971-2035 and 2036-2100.

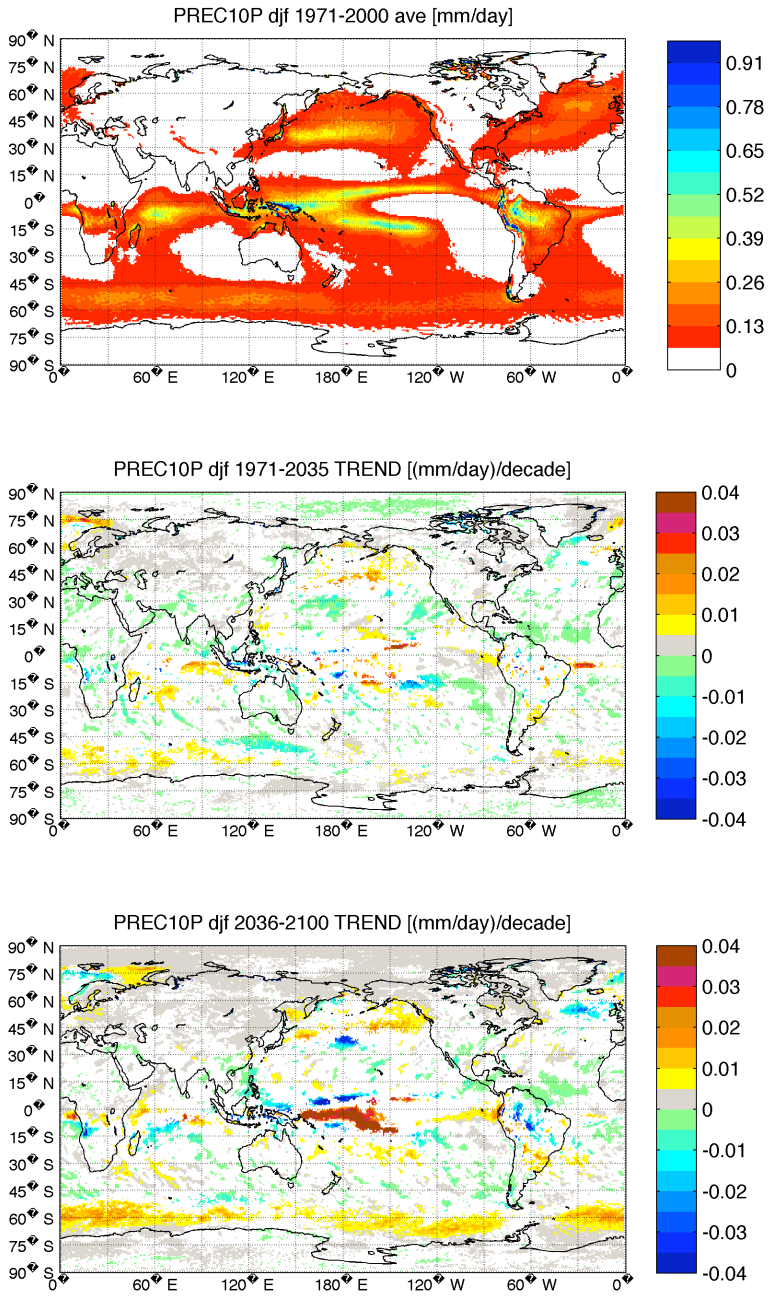

Figure 13:
PREC10P index computed for DJF season: 10^{th} percentile of the daily precipitation. The first panel shows the average of this index over the 1971-2100 considered period. The last two panes show the index linear trend during 1971-2035 and 2036-2100. White patterns identify grid points where the computed trend is not statistically significant.

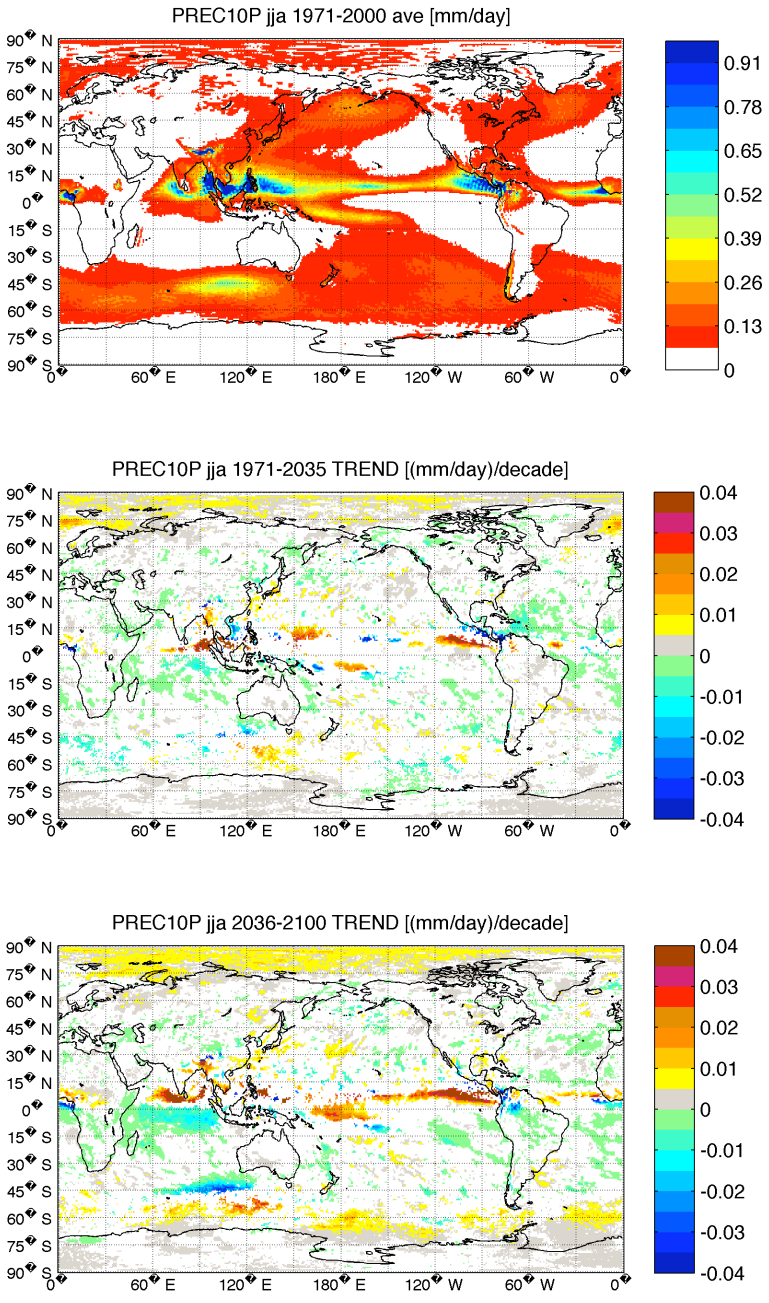

Figure 14:
PREC10P index computed for JJA season: 10^{th} percentile of the daily precipitation. The first panel shows the average of this index over the 1971-2100 considered period. The last two panes show the index linear trend during 1971-2035 and 2036-2100. White patterns identify grid points where the computed trend is not statistically significant.

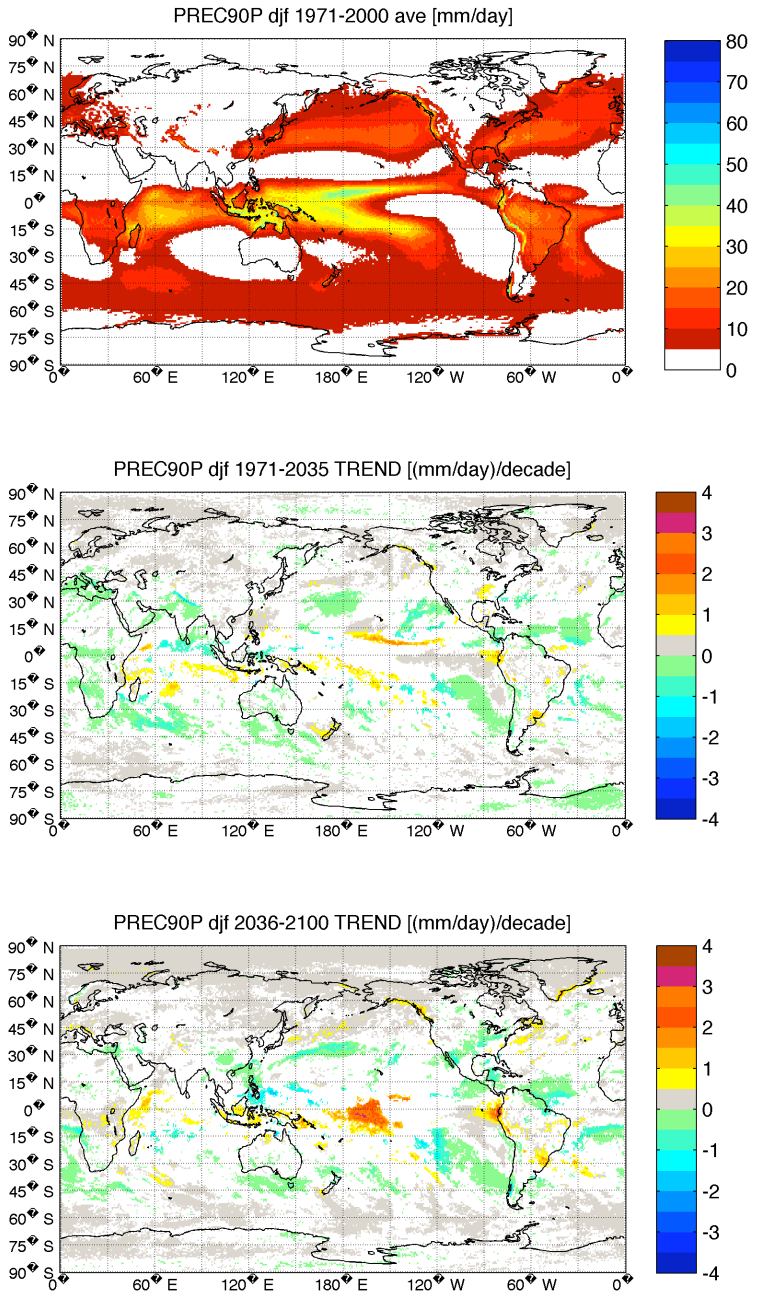

Figure 15:
PPREC90P index computed for DJF season: 90^{th} percentile of the daily precipitation. The first panel shows the average of this index over the 1971-2100 considered period. The last two panes show the index linear trend during 1971-2035 and 2036-2100. White patterns identify grid points where the computed trend is not statistically significant.

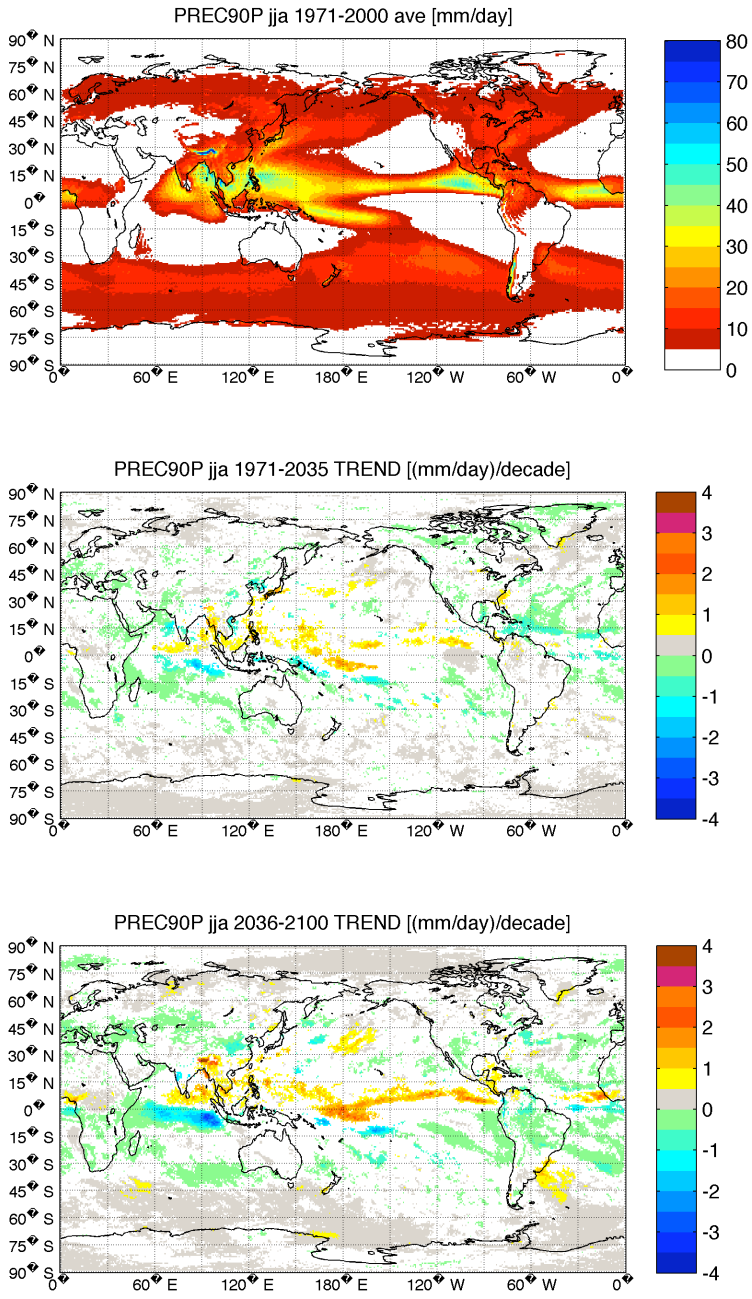

Figure 16:
PREC90P index computed for JJA season: 90^{th} percentile of the daily precipitation. The first panel shows the average of this index over the 1971-2100 considered period. The last two panes show the index linear trend during 1971-2035 and 2036-2100. White patterns identify grid points where the computed trend is not statistically significant.

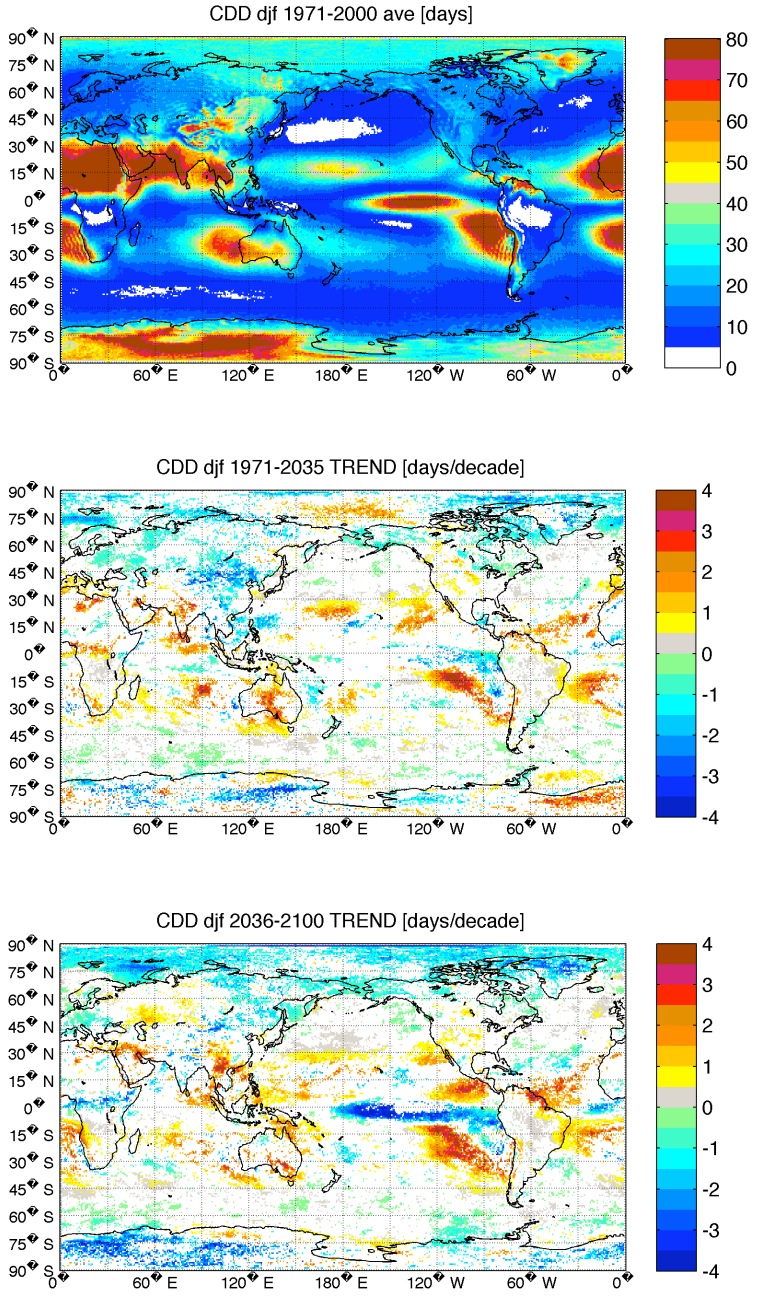

Figure 17:
CDD index computed for DJF season: Maximum number of consecutive dry days (defined as precip <= 1 mm/day). The first panel shows the average of this index over the 1971-2000 considered period. The last two panes show the index linear trend during 1971-2035 and 2036-2100. White patterns identify grid points where the computed trend is not statistically significant.

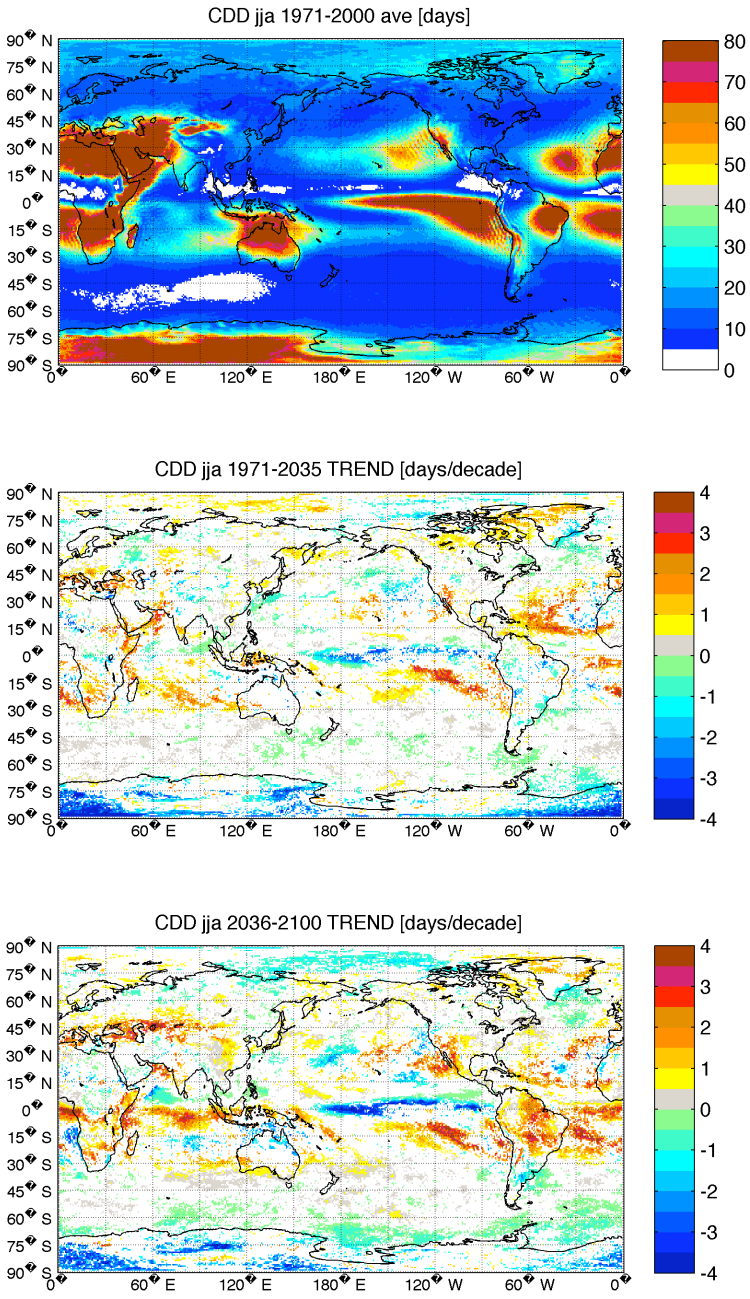

Figure 18:
CDD index computed for JJA season: Maximum number of consecutive dry days (defined as precip <= 1 mm/day). The first panel shows the average of this index over the 1971-2000 considered period. The last two panes show the index linear trend during 1971-2035 and 2036-2100. White patterns identify grid points where the computed trend is not statistically significant.

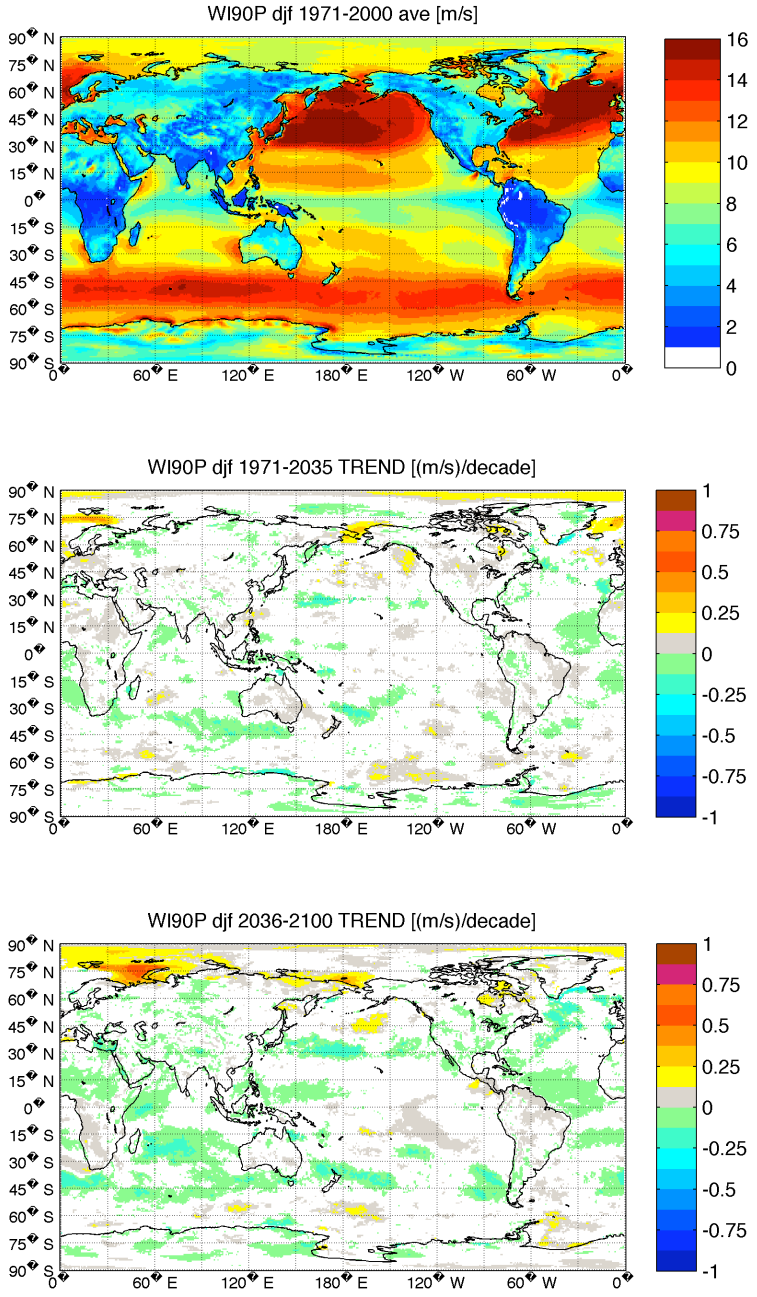

Figure 19:
WI90P index computed for DJF season: 90^{th} percentile of the 10m wind speed. The first panel shows the average of this index over the 1971-2000 considered period. The last two panes show the index linear trend during 1971-2035 and 2036-2100. White patterns identify grid points where the computed trend is not statistically significant.

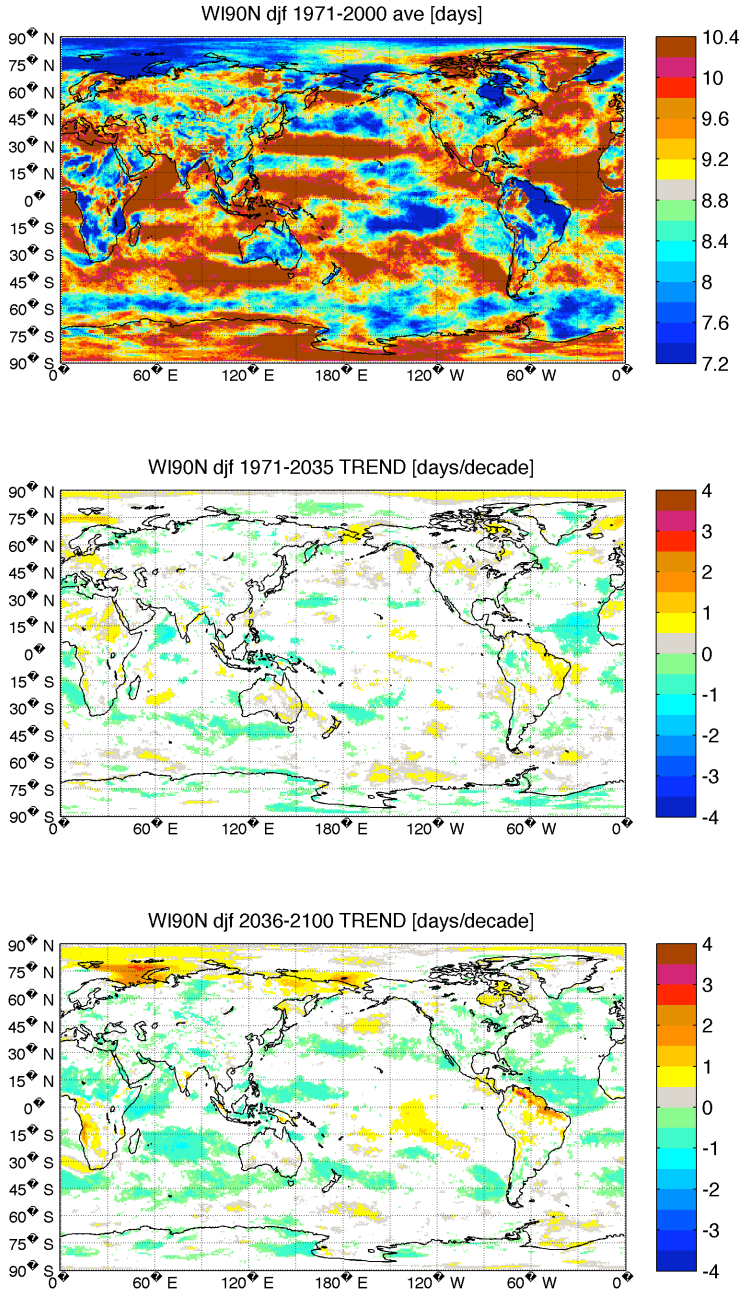

Figure 20:
WI90N index computed for DJF season: number of days with daily 10m wind speed exceeding the long term 90^{th} percentile of the 10m wind speed. The first panel shows the average of this index over the 1971-2000 considered period. The last two panes show the index linear trend during 1971-2035 and 2036-2100. White patterns identify grid points where the computed trend is not statistically significant.

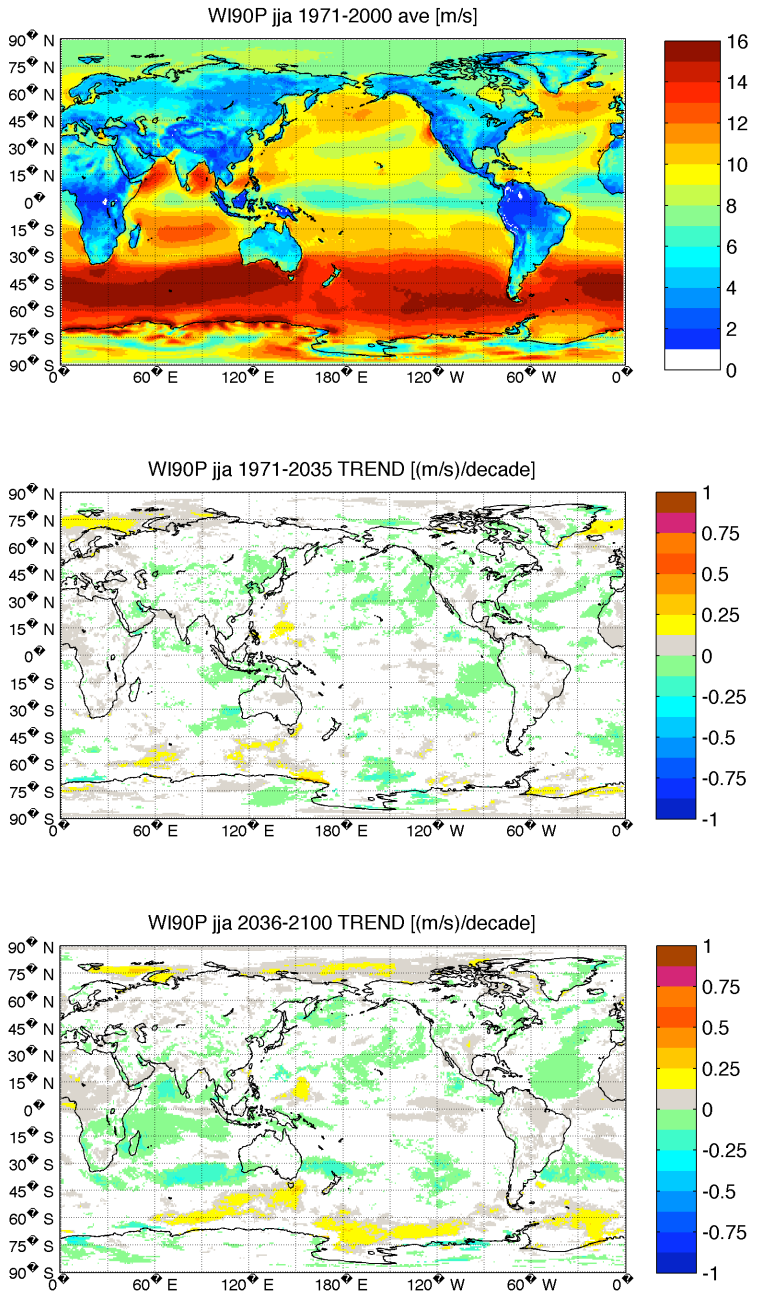

Figure 21:
WI90P index computed for JJA season: 90^{th} percentile of the 10m wind speed. The first panel shows the average of this index over the 1971-2000 considered period. The last two panes show the index linear trend during 1971-2035 and 2036-2100. White patterns identify grid points where the computed trend is not statistically significant.

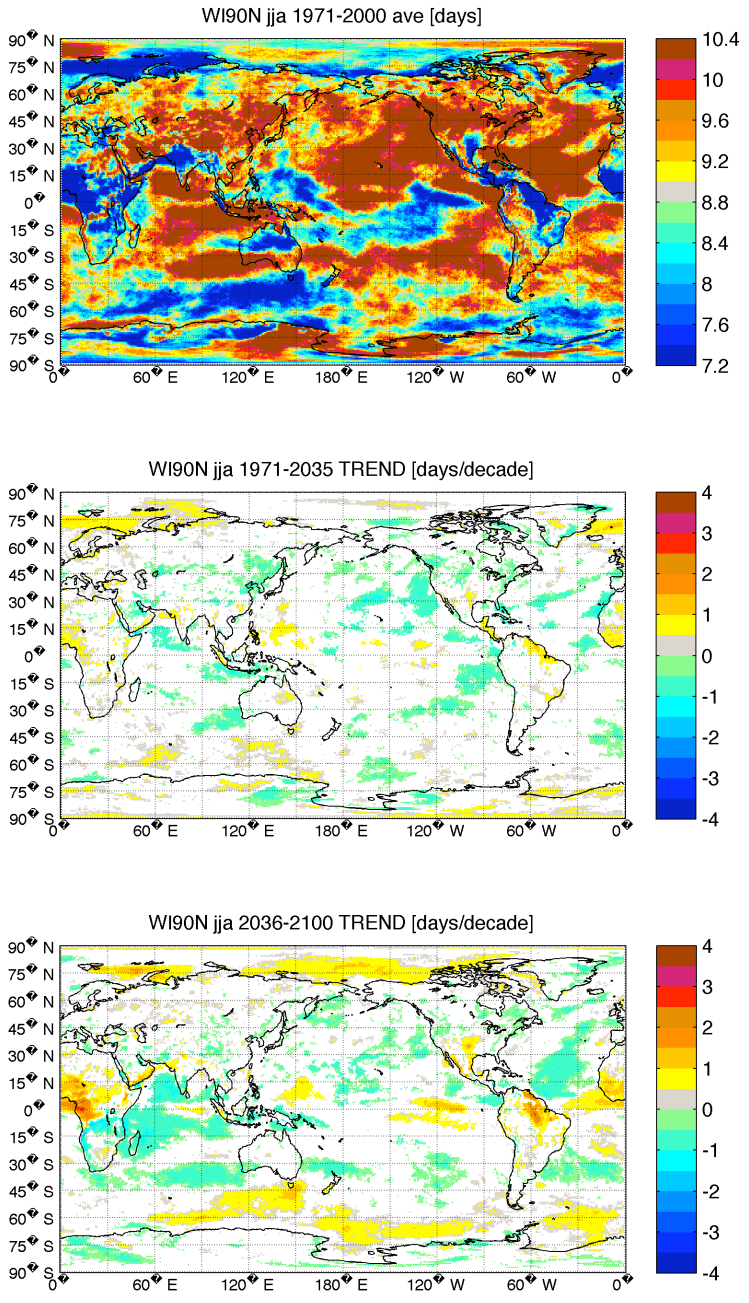

Figure 22:
WI90N index computed for JJA season: number of days with daily 10m wind speed exceeding the long term 90^{th} percentile of the 10m wind speed. The first panel shows the average of this index over the 1971-2000 considered period. The last two panes show the index linear trend during 1971-2035 and 2036-2100. White patterns identify grid points where the computed trend is not statistically significant.

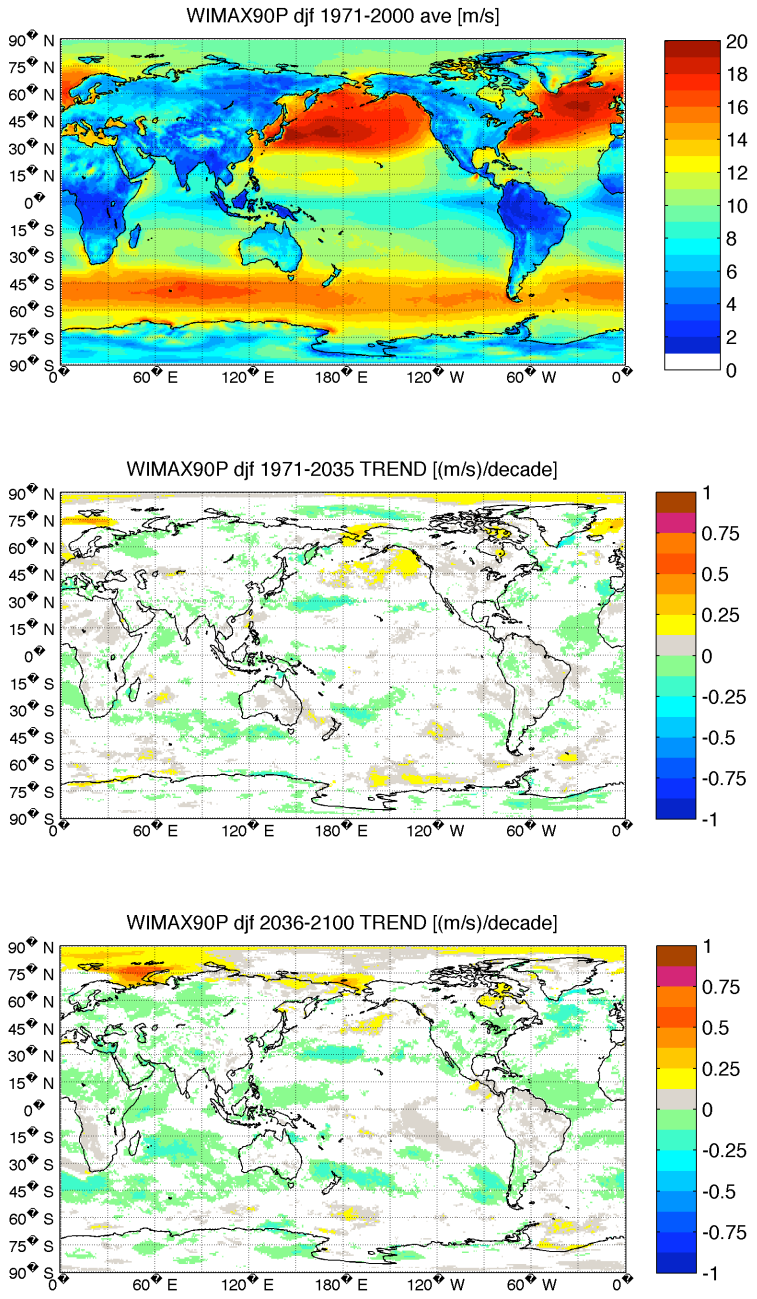

Figure 23:
WIMAX90P index computed for DJF season: 90^{th} percentile of the 10m maximum wind speed. The first panel shows the average of this index over the 1971-2000 considered period. The last two panes show the index linear trend during 1971-2035 and 2036-2100. White patterns identify grid points where the computed trend is not statistically significant.

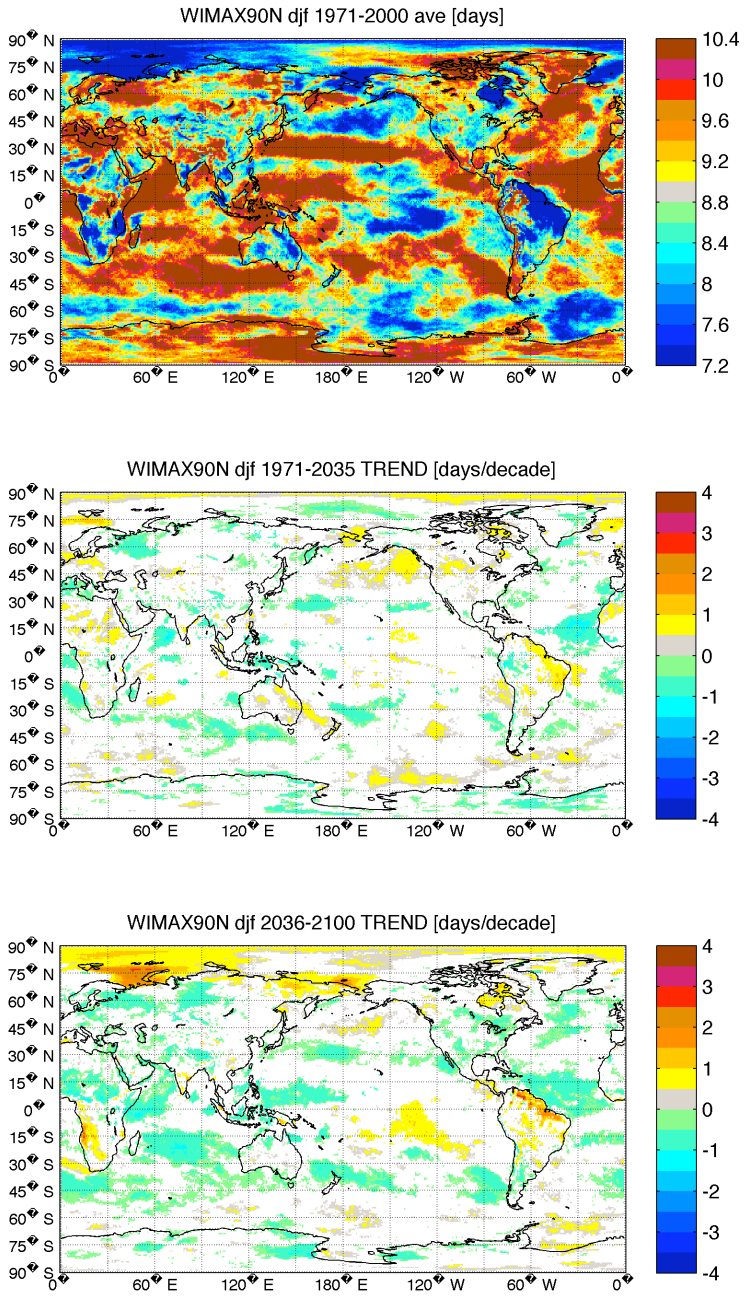

Figure 24:
WIMAX90N index computed for DJF season: number of days with daily 10m wind speed exceeding the long term 90^{th} percentile of the 10m maximum wind speed. The first panel shows the average of this index over the 1971-2000 considered period. The last two panes show the index linear trend during 1971-2035 and 2036-2100. White patterns identify grid points where the computed trend is not statistically significant.

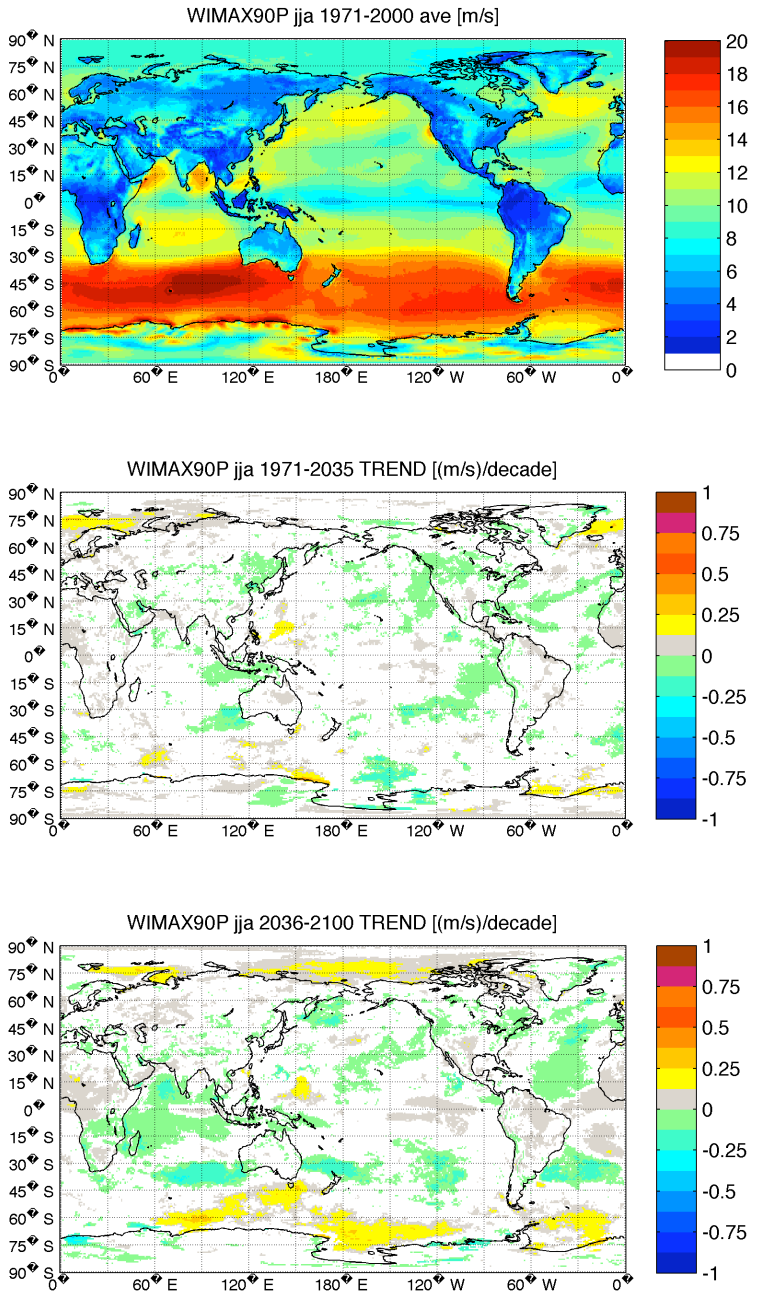

Figure 25:
WIMAX90P index computed for JJA season: 90^{th} percentile of the maximum 10m wind speed. The first panel shows the average of this index over the 1971-2000 considered period. The last two panes show the index linear trend during 1971-2035 and 2036-2100. White patterns identify grid points where the computed trend is not statistically significant.

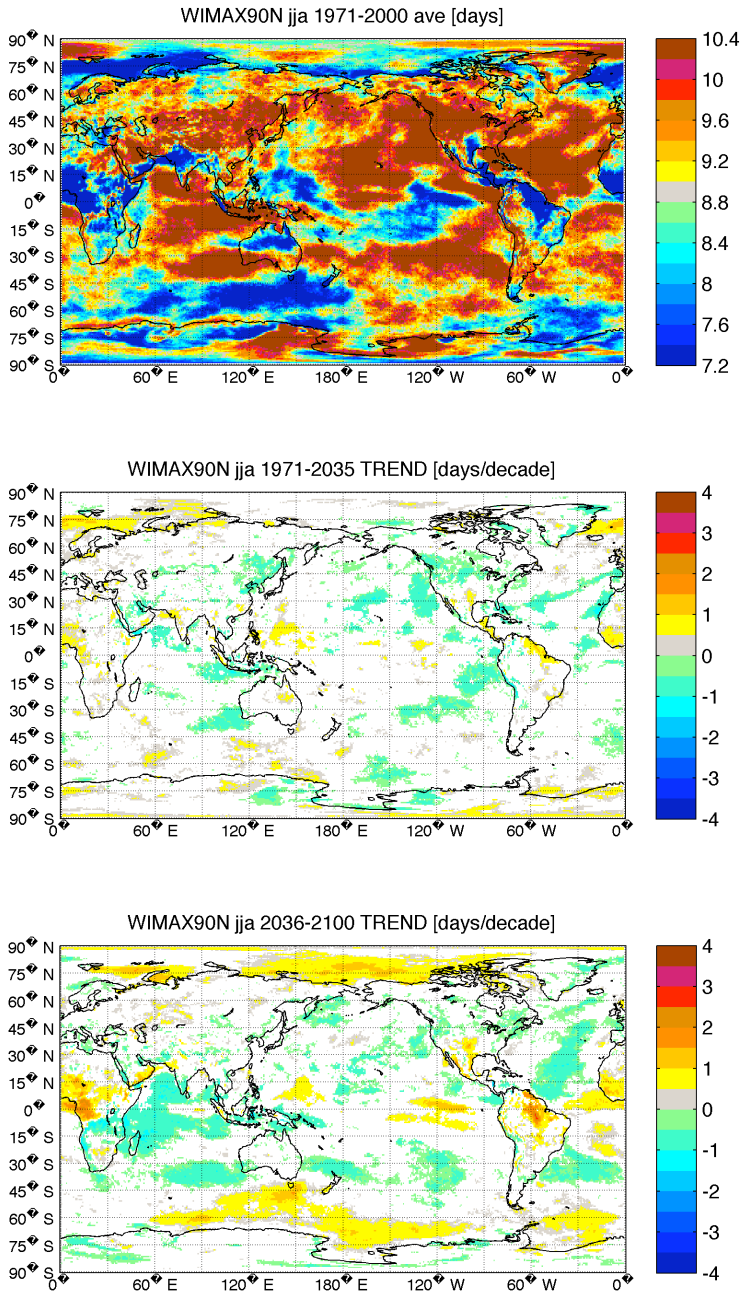

Figure 26:
WIMAX90N index computed for JJA season: number of days with daily 10m maximum wind speed exceeding the long term 90^{th} percentile of the 10m wind speed. The first panel shows the average of this index over the 1971-2000 considered period. The last two panes show the index linear trend during 1971-2035 and 2036-2100. White patterns identify grid points where the computed trend is not statistically significant.

5 Extreme events at regional scale

In this section we discuss the extreme indexes computed over the Euro-Mediterranean with the regional model and, for the sake of brevity, we consider only the DJF and JJA seasons.

5.1 Temperature

The seasonal average of minimum daily temperature (MEANTN), averaged over the first 30 simulated years (1971-2000) is shown in the top panel of figure 27 (MEANTN, DJF) and figure 28 (MEANTN, JJA). In both seasons the minimum MEANTN values are found over the Alps and the maximum values are found over the southern Atlantic box and south-eastern part of the Mediterranean Sea during DJF, and over North Africa in JJA. In DT1 period small MEANTN positive trends (less than 0.2^{o}C/decade, yellow patterns in figures 27 and 28, middle panels) are extended to all the mediterranean domain except for the eastern Europe during JJA. In DT2 there are large regions reaching trends of 0.5^{o}C/decade (red patterns in figures 27 and 28 last panels) over Turkey and eastern Europe in both seasons, and also over Spain, Morocco and Algeria during JJA. These positive patterns in MEANTN trends are confirmed by 10^{th} percentile of the daily minimum temperature (TN10P) that shows similar but more pronounced trend patterns (figures 29 and 30), with maxima reaching 1^{o}C/decade north to the Black Sea. The maximum daily temperature (MEANTX, figure 31 and 32) shows tendencies similar to the MEANTN, but with some distinguished features: the region showing not significant trend over eastern Europe in DT1 during JJA (Figure 28 middle panel) is now associated to a small negative pattern (Figure 32, panel 2) and during DT2, in the same season, the region with high trends (0.5^{o}C/decade) is more extended with respect to the one found in MEANTN, over France and northern part of Italy. The 90^{th} percentile of the daily maximum temperature (TX90P, figures 33 and 34) confirms the tendencies shown by MEANTX, with a maximum trend of 1^{o}C/decade over France. In summary, in terms of extremely low temperature events (TN10P, DJF, figure 29) the model shows a tendency to warmer events (positive trends shown in figure 29, last two panels) in future climate. On the other hand, also in terms of extremely high temperature events the model shows a tendency to warmer events (positive trends shown in figure 34, last two panels) despite an anomalous tendency to colder events over a small region north of the Black Sea in summer during DT1 (negative trends shown in figure 32, middle panel). The anomalous tendency north of Black Sea in MEANTX is confirmed by the 90^{th} percentile of the daily maximum temperature (Figure 34 middle panel).

The total number of consecutive days with maximum daily temperature exceeding the long term (1971-2100) 90^{th} percentile (WSDI90, figures 35 and 36) highlight the tendency to have hot periods: during DT1 small trends interest the Euro-Mediterranean area with few regions affected also by negative trends, especially in JJA (figure 36, middle panel); during DT2 the entire spatial domain is affected by positive trends in both seasons. This summer positive trend from 2036 onward has its maximum over the Balearic Sea in JJA reaching 4 days/decade. Positive trends in WSDI90 are less pronounced over the continents with respect to the oceans. The CSDI10 (total number of consecutive days with minimum daily temperature below the long term 10^{th} percentile) index, useful to investigate the tendency to have extreme cold periods, is shown in figure 37 (CSDI10, DJF) and 38 (CSDI10, JJA): the trend

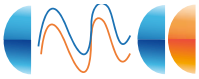

is small and negative, with a more pronounced signal during DT1 with respect to DT2 in both seasons. It is interesting to note that in DT1, during JJA no significant trends are found in CSDI10 index over almost the entire European land covered domain.

5.2 Precipitation

In terms of extremely low precipitation events (PREC10P, figures 39 and 40) the model shows almost no tendencies in both seasons (DJF and JJA) and periods (DT1 and DT2), except for summer in DT2 when, over the Alps, a slightly pronounced, negative pattern is found. Extremely high precipitation events (PREC90P, figures 41 and 42) shows almost no trends over the sea in both period and very different tendencies over land in the two considered seasons. During DJF positive trends, up to 0.8 (mm/day)/decade, are found over the Alps and other smaller areas (e.g. south and west of the Black sea) in DT1. Also negative trends, with comparable magnitude, are found in the same period over coastal areas in Morocco, Algeria and northern Spain (Figure 41, middle panel). During DT2 the positive trend over the Alps is reinforced and involves now a wider region (e.g. Balkans and eastern part of France). On the other hand, during JJA, the north-eastern part of the domain exhibits a positive trend up to 0.9 (mm/day)/decade in DT1 and a wide regions with negative trend in DT2 over Pyrenees, France, Alps and Balkans. The tendency to drought-like condition during DJF seems to increase under the DT1 period over Spain, Morocco and part of northern Algeria, as revealed by red patterns in Figure 43, middle panel. This tendency disappears in DT2 when a negative trend pattern becomes evident over the Alps and a positive tendency is found over northern Egypt (Figure 43, bottom panel), a region where drought conditions are evident also during winter (Figure 43, top panel). In JJA, the most prone season to drought conditions, the only well defined trend pattern during DT1 is over the north western Black Sea (Figure 44, middle panel). During DT2 a positive, patchy pattern covers a substantial part of the domain with maxima over the north-eastern part of Turkey.

5.3 Winds

The 90^{th} percentile of wind speed at 10 meter (WI90P index) averaged over 1971-2000 shows maximum values during winter season (DJF, figure 45, top panel) over the sea. Over the land covered surface there are no substantial differences between DJF and JJA in the averaged WI90P index (Figure 45 and 47, top panel). In both seasons (DJF and JJA) and periods (DT1 and DT2) there are no WI90P sizeable tendencies over land. On the other hand significant tendency are found in the number of days with daily 10m wind speed exceeding the long term 90^{th} percentile of the 10m wind speed (WI90N): over northern Egypt and Europe north of 45^{o}N, a positive trend reaching 0.075 days/y, leading to 5 days after 65 years, is found in DT1 during DJF. The positive trend pattern over Egypt Is confirmed in JJA but the positive tendency over Europe disappears in this season. These WI90N tendencies are not confirmed in DT2 when the index seems to be almost constant, at list over the major part of land covered domain. The tendencies found over land in 10 meter daily averaged wind indexes are confirmed by percentiles computed on gusts (WIMAX90P and WIMAX90N) as shown in Figures 49, 50, 51 and 52.

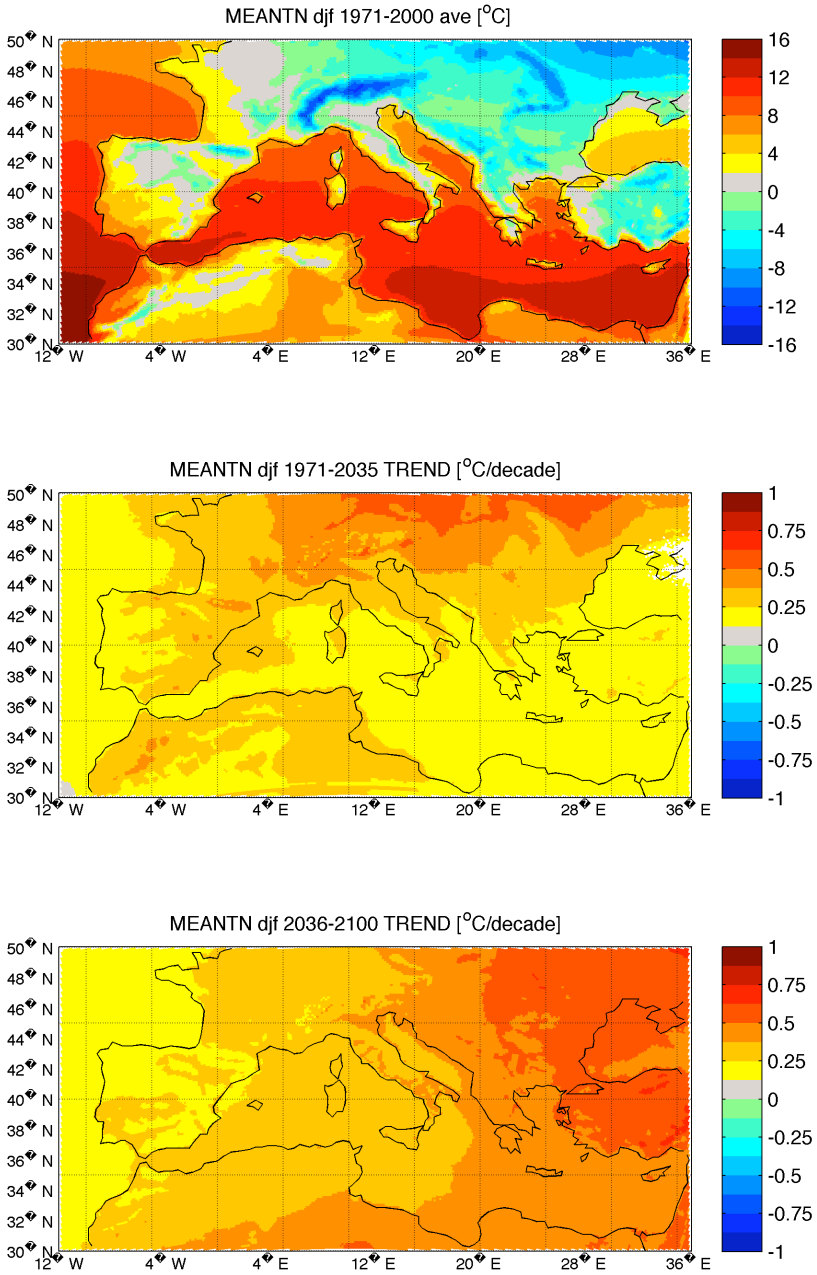

Figure 27:
MEANTN index computed for DJF season: seasonal average of daily minimum temperature. The first panel shows the average of this index over the 1971-2000 considered period. The last two panes show the index linear trend during 1971-2035 and 2036-2100. White patterns identify grid points where the computed trend is not statistically significant

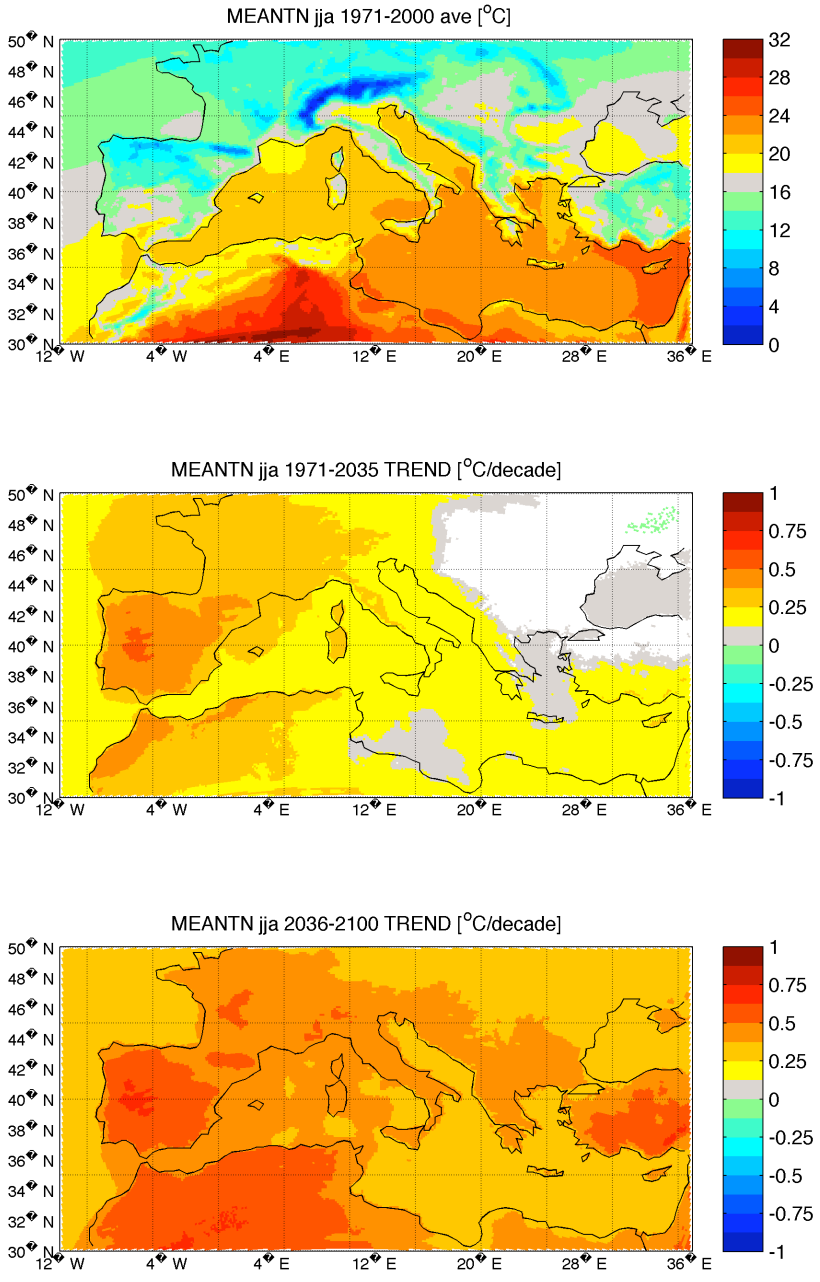

Figure 28:
MEANTN index computed for JJA season: seasonal average of daily minimum temperature. The first panel shows the average of this index over the 1971-2000 considered period. The last two panes show the index linear trend during 1971-2035 and 2036-2100. White patterns identify grid points where the computed trend is not statistically significant

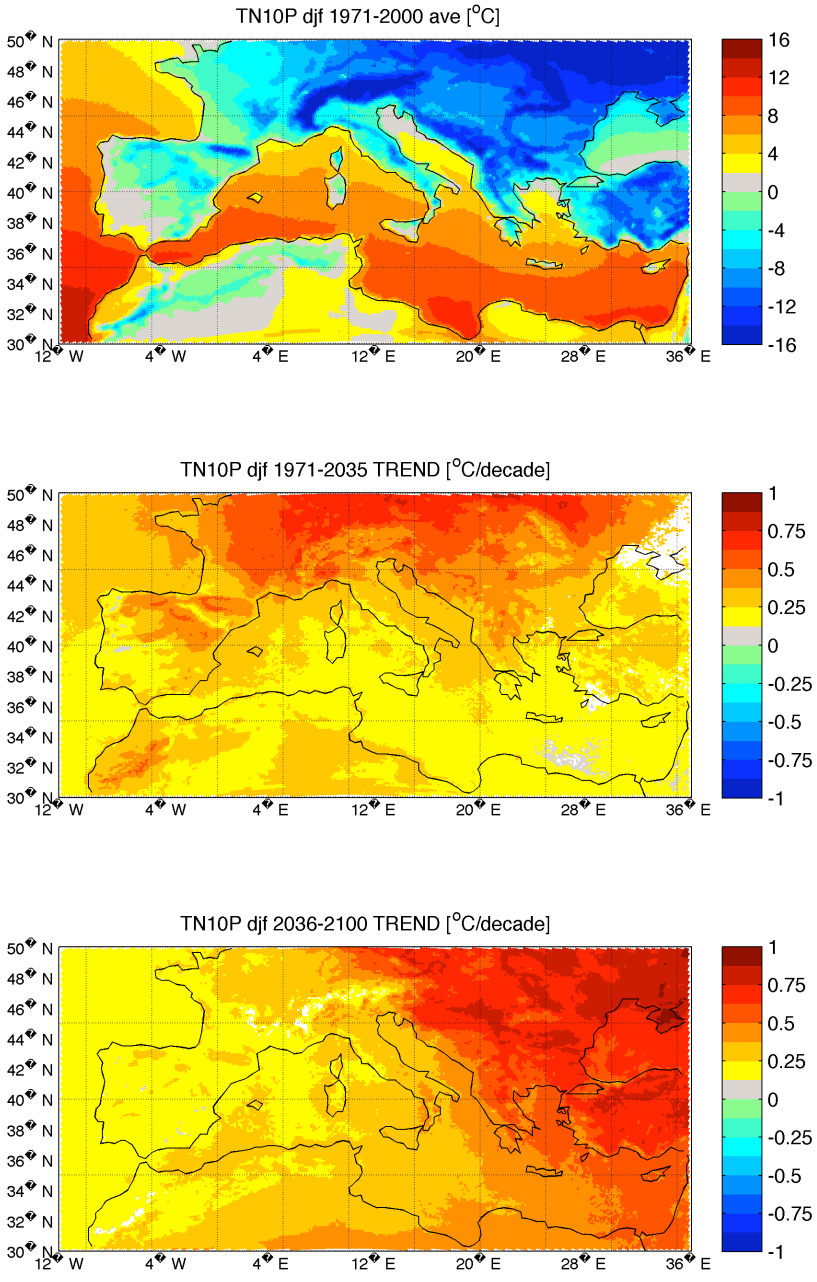

Figure 29:
TN10P index computed for DJF season: 10^{th} percentile of the daily minimum temperature. The first panel shows the average of this index over the 1971-2000 considered period. The last two panes show the index linear trend during 1971-2035 and 2036-2100. White patterns identify grid points where the computed trend is not statistically significant

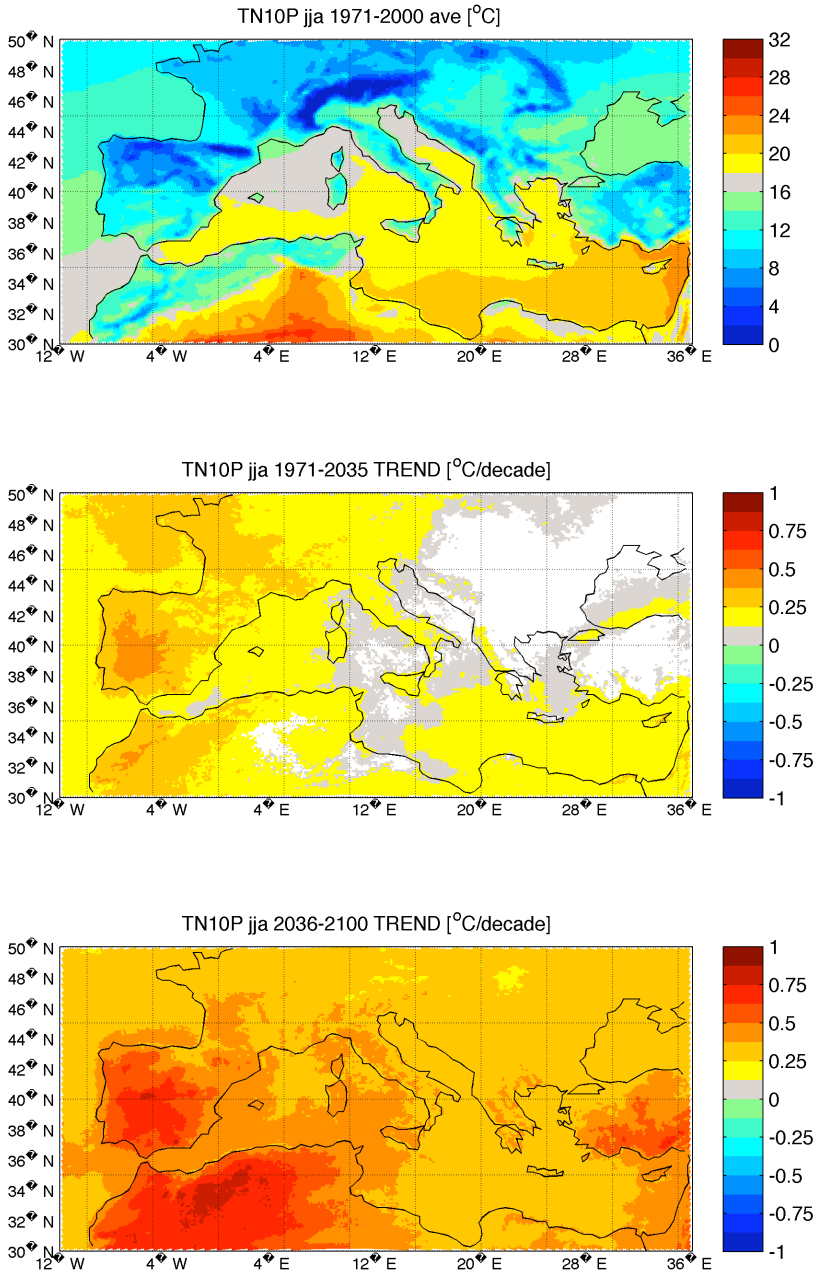

Figure 30:
TN10P index computed for JJA season: 10^{th} percentile of the daily minimum temperature. The first panel shows the average of this index over the 1971-2000 considered period. The last two panes show the index linear trend during 1971-2035 and 2036-2100. White patterns identify grid points where the computed trend is not statistically significant

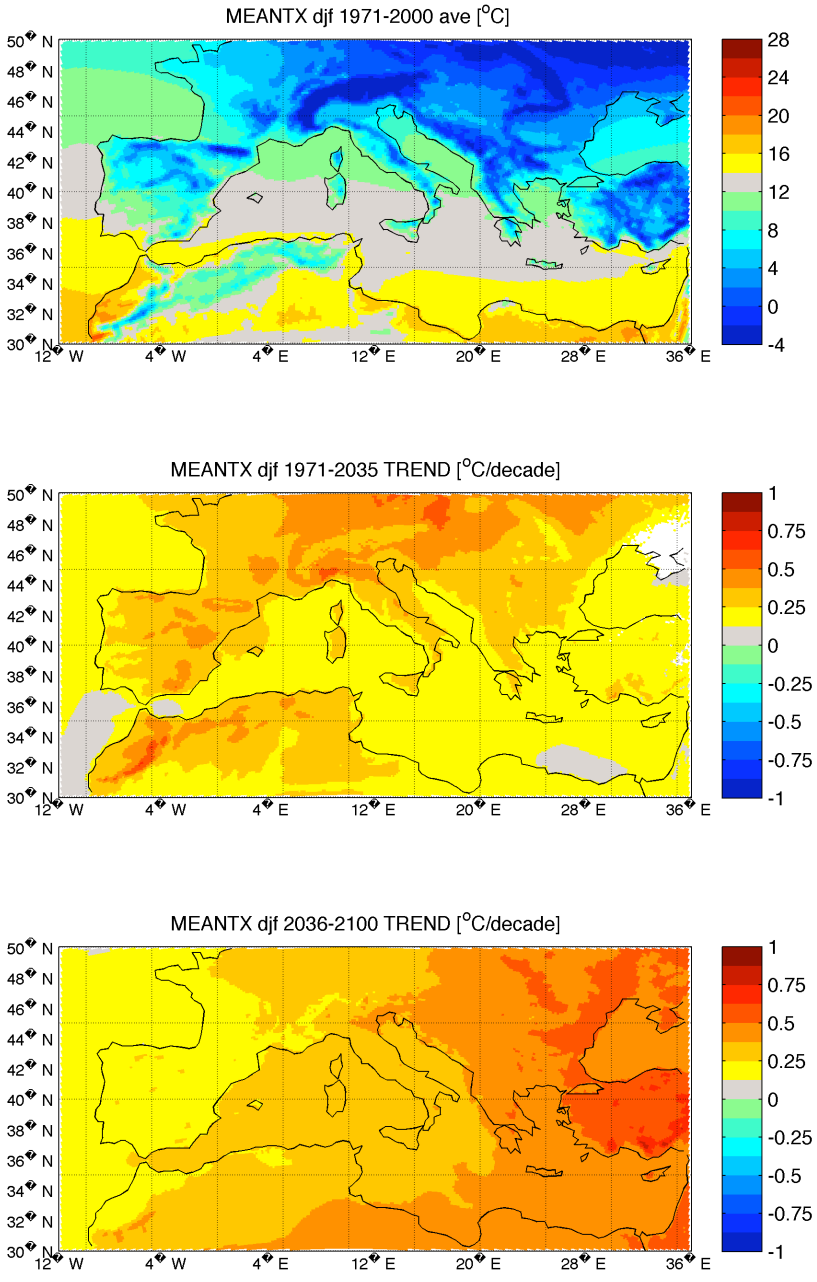

Figure 31:
MEANTX index computed for DJF season: seasonal average of daily maximum temperature. The first panel shows the average of this index over the 1971-2000 considered period. The last two panes show the index linear trend during 1971-2035 and 2036-2100. White patterns identify grid points where the computed trend is not statistically significant.

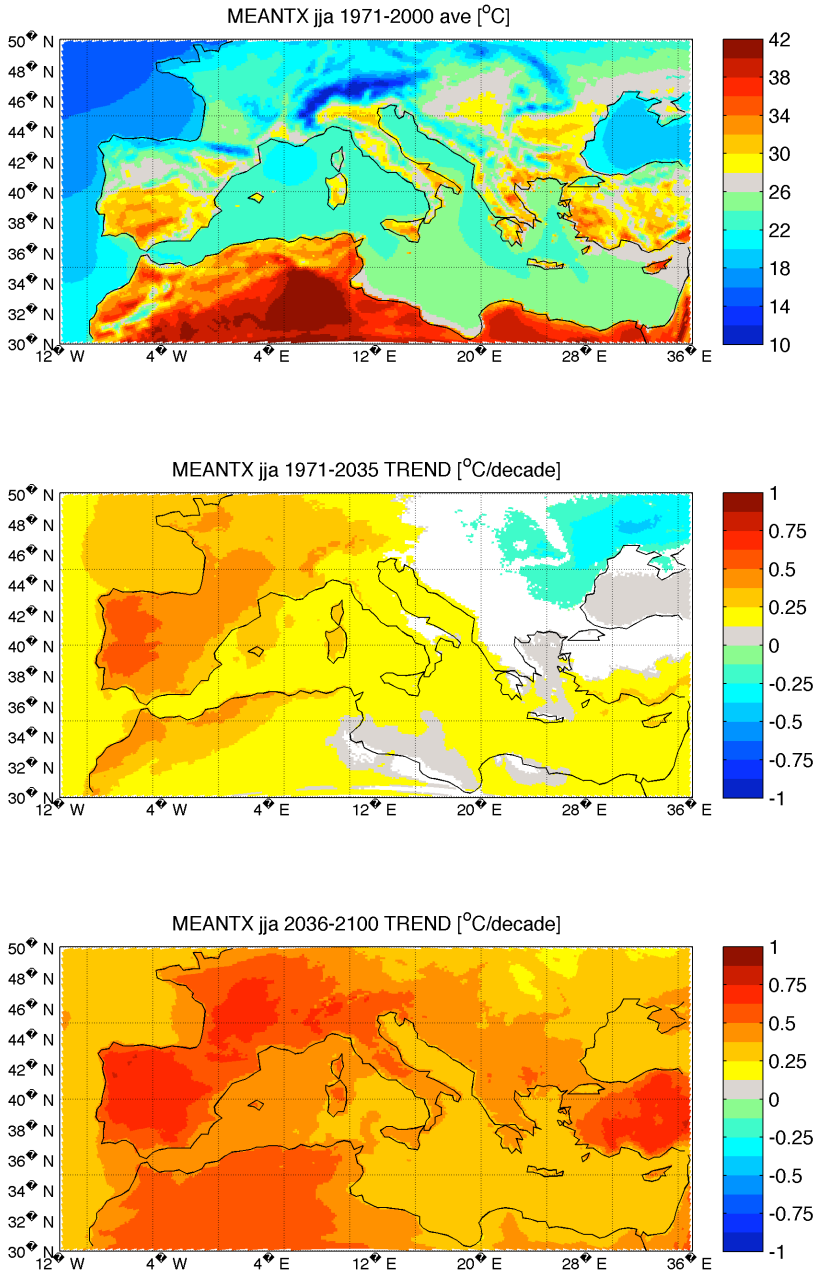

Figure 32:
MEANTX index computed for JJA season: seasonal average of daily maximum temperature. The first panel shows the average of this index over the 1971-2000 considered period. The last two panes show the index linear trend during 1971-2035 and 2036-2100. White patterns identify grid points where the computed trend is not statistically significant.

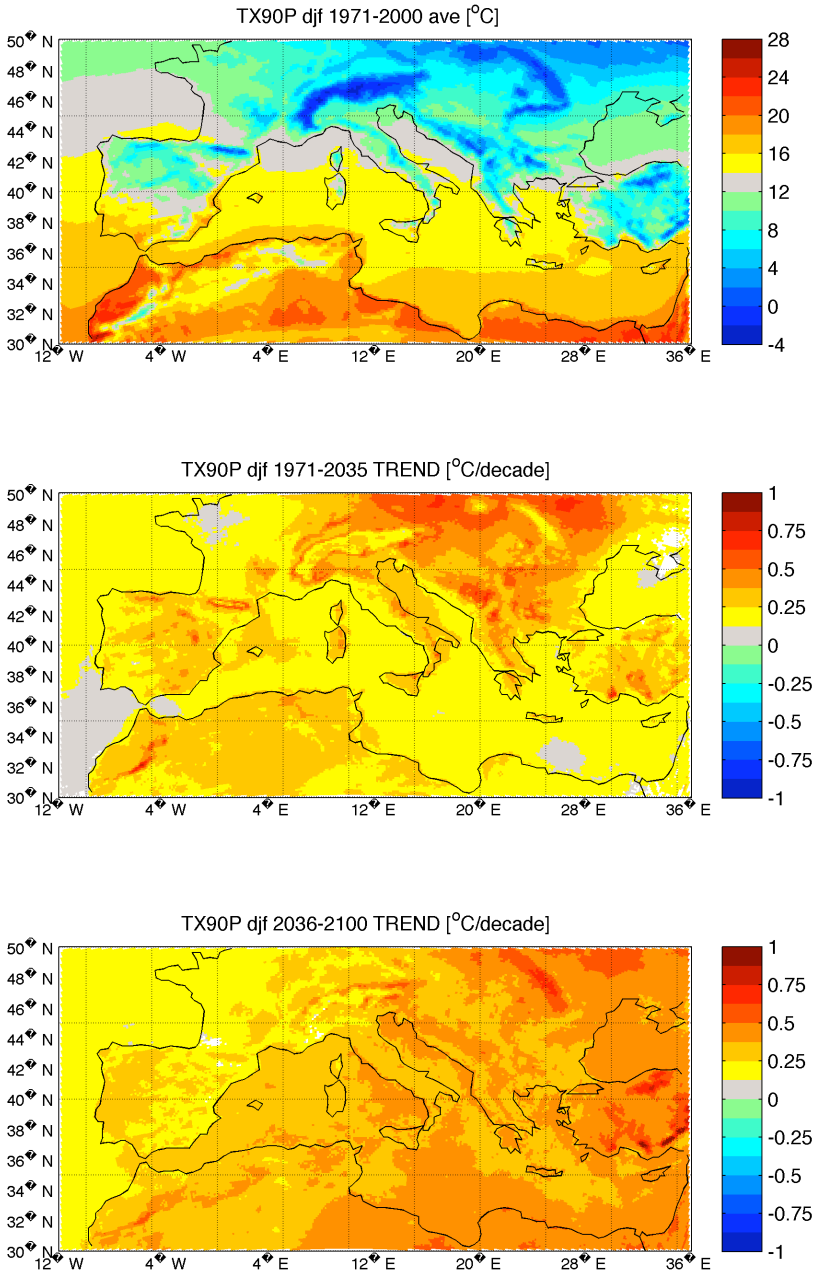

Figure 33:
TX90P index computed for DJF season: 90^{th} percentile of the daily maximum temperature. The first panel shows the average of this index over the 1971-2000 considered period. The last two panes show the index linear trend during 1971-2035 and 2036-2100. White patterns identify grid points where the computed trend is not statistically significant.

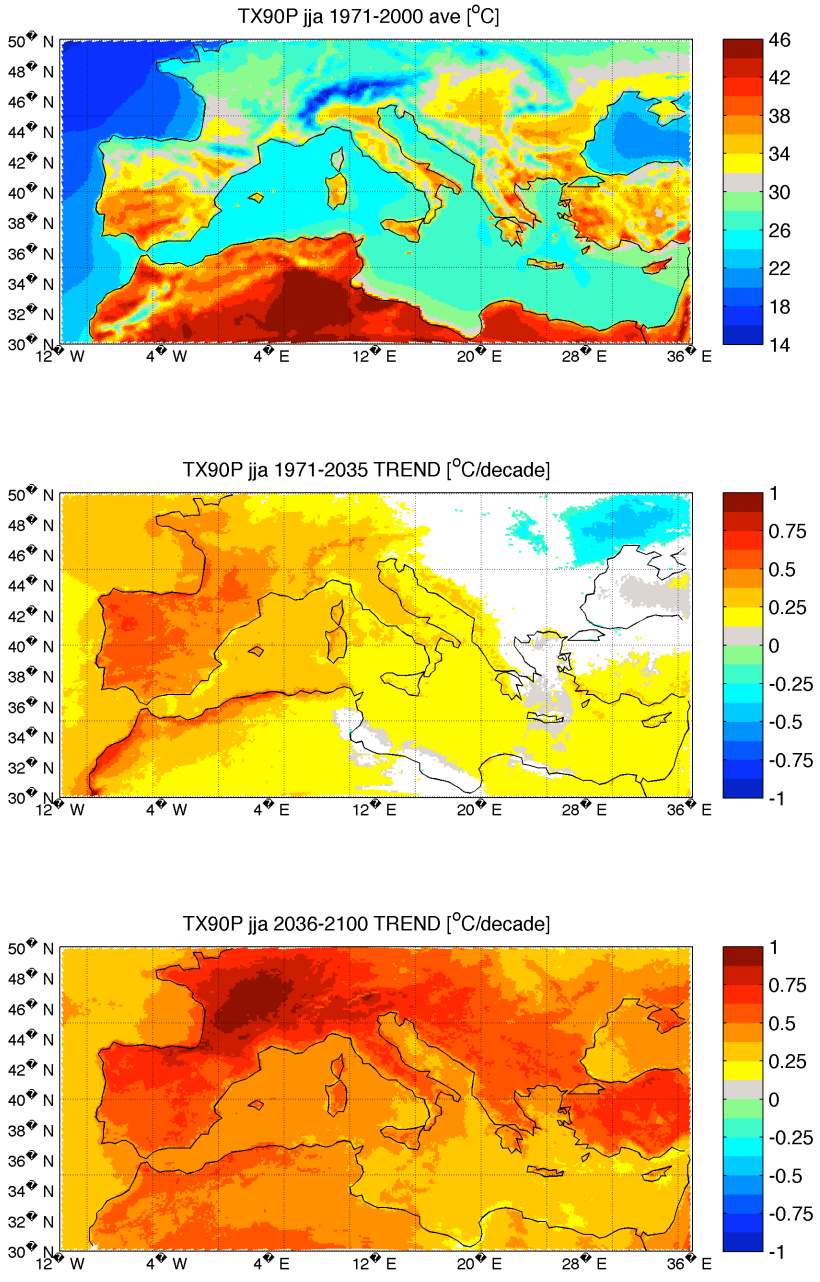

Figure 34:
TX90P index computed for JJA season: 90^{th} percentile of the daily maximum temperature. The first panel shows the average of this index over the 1971-2000 considered period. The last two panes show the index linear trend during 1971-2035 and 2036-2100. White patterns identify grid points where the computed trend is not statistically significant.

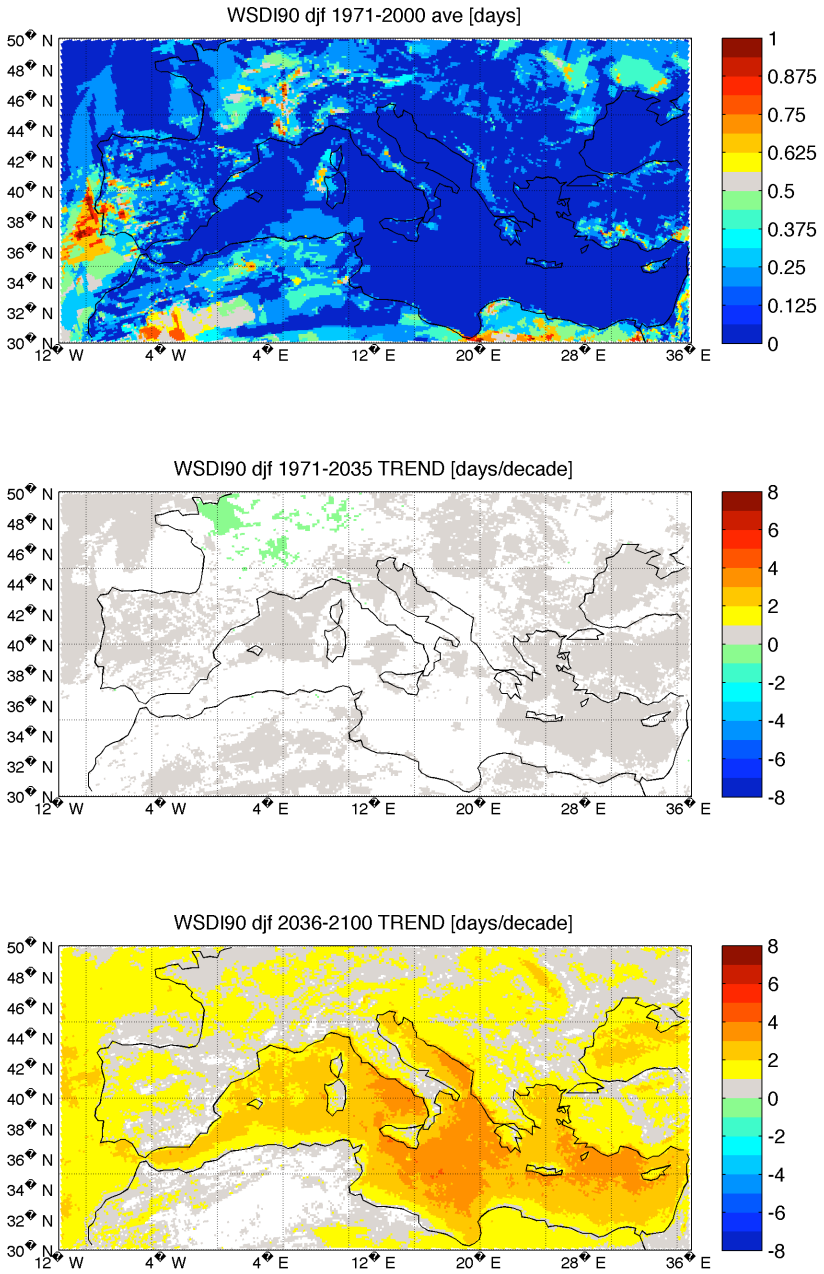

Figure 35:
WSDI90 index computed for DJF season: total number of consecutive days with maximum daily temperature exceeding the long term (1971-2100) 90^{th} percentile. The first panel shows the average of this index over the 1971-2000 considered period. The last two panes show the index linear trend during 1971-2035 and 2036-2100.

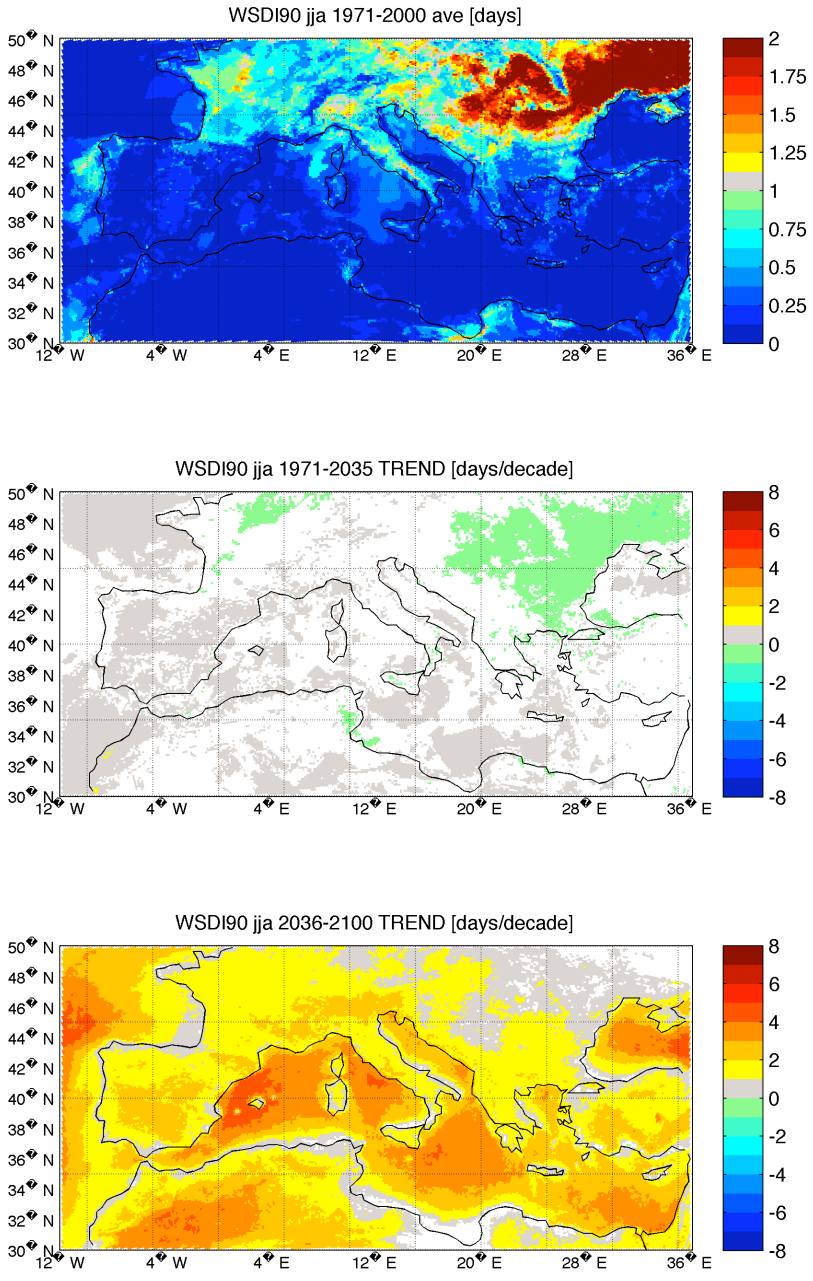

Figure 36:
WSDI90 index computed for JJA season: total number of consecutive days with maximum daily temperature exceeding the long term (1971-2000) 90^{th} percentile. The first panel shows the average of this index over the 1971-2100 considered period. The last two panes show the index linear trend during 1971-2035 and 2036-2100.

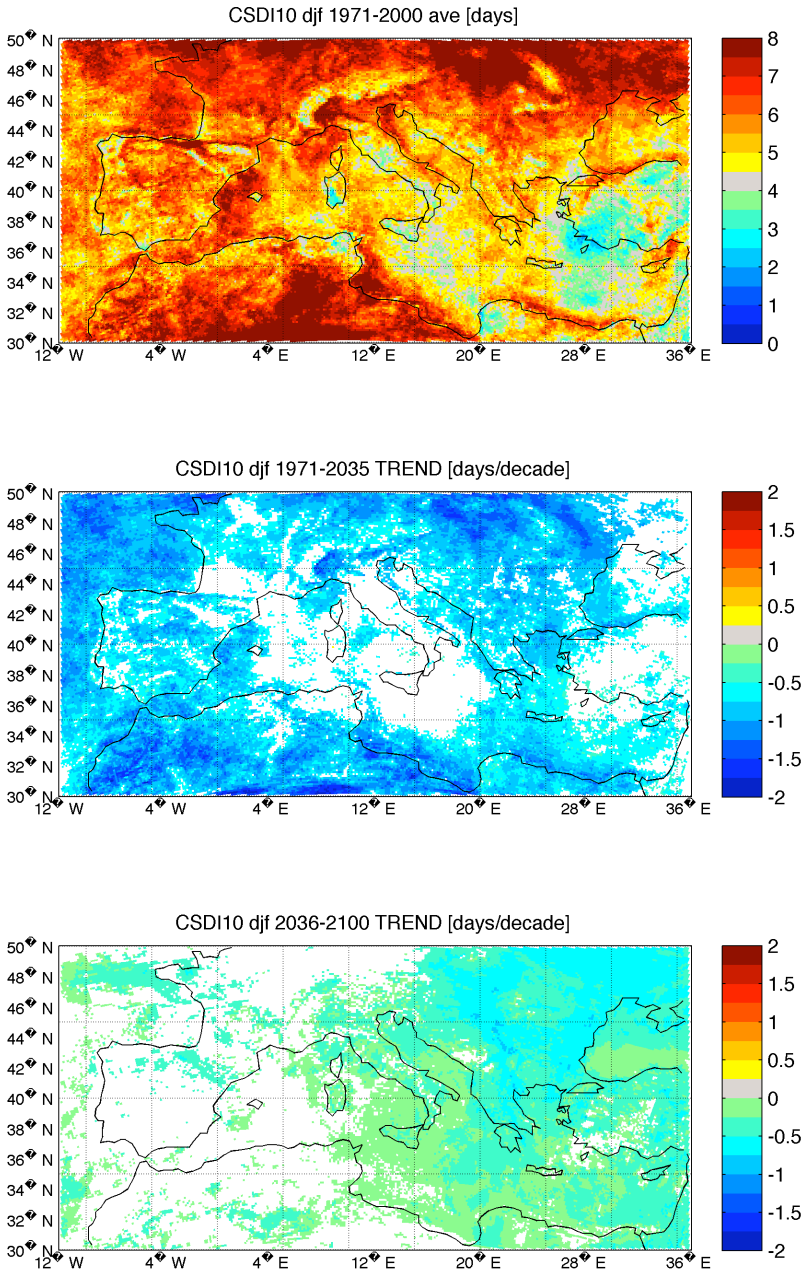

Figure 37:
CSDI10 index computed for DJF season: total number of consecutive days with minimum daily temperature below the long term (1971-2000) 10^{th} percentile. The first panel shows the average of this index over the 1971-2100 considered period. The last two panes show the index linear trend during 1971-2035 and 2036-2100.

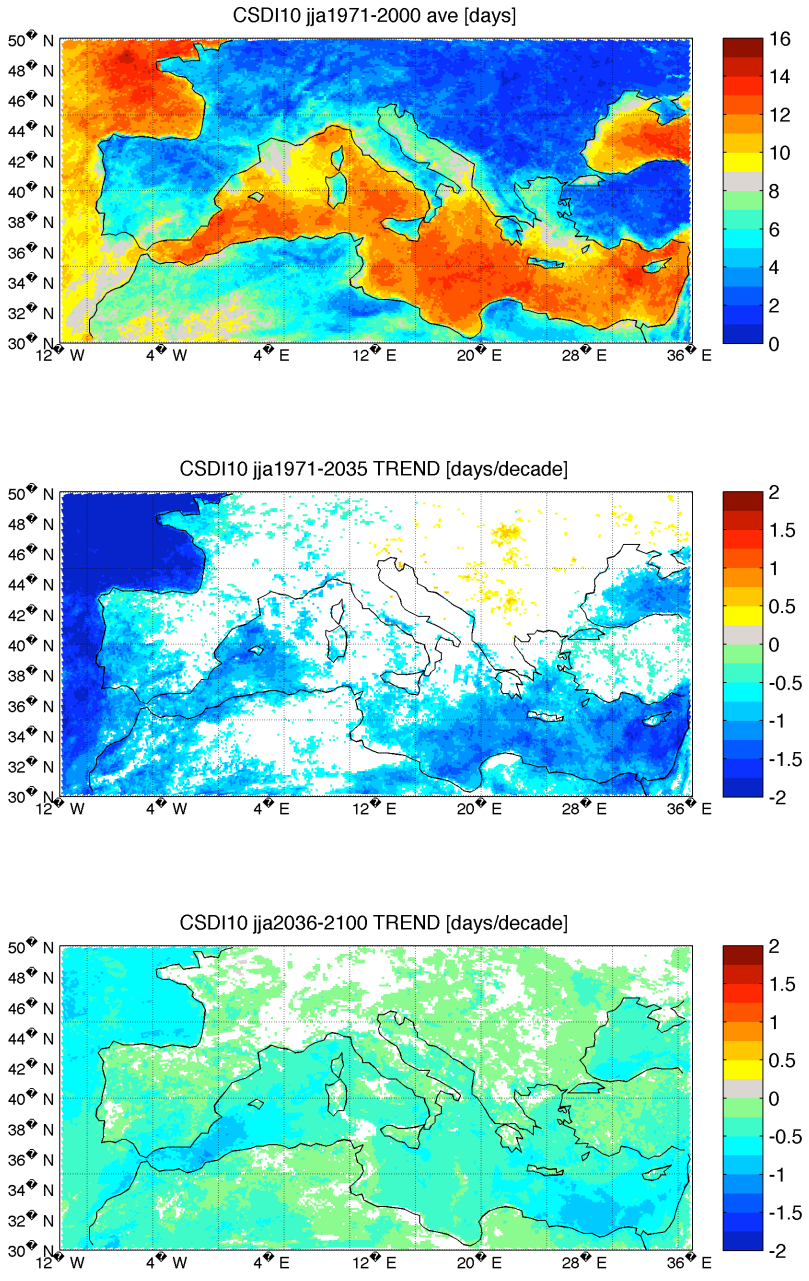

Figure 38:
CSDI10 index computed for JJA season: total number of consecutive days with minimum daily temperature below the long term (1971-2000) 10^{th} percentile. The first panel shows the average of this index over the 1971-2100 considered period. The last two panes show the index linear trend during 1971-2035 and 2036-2100.

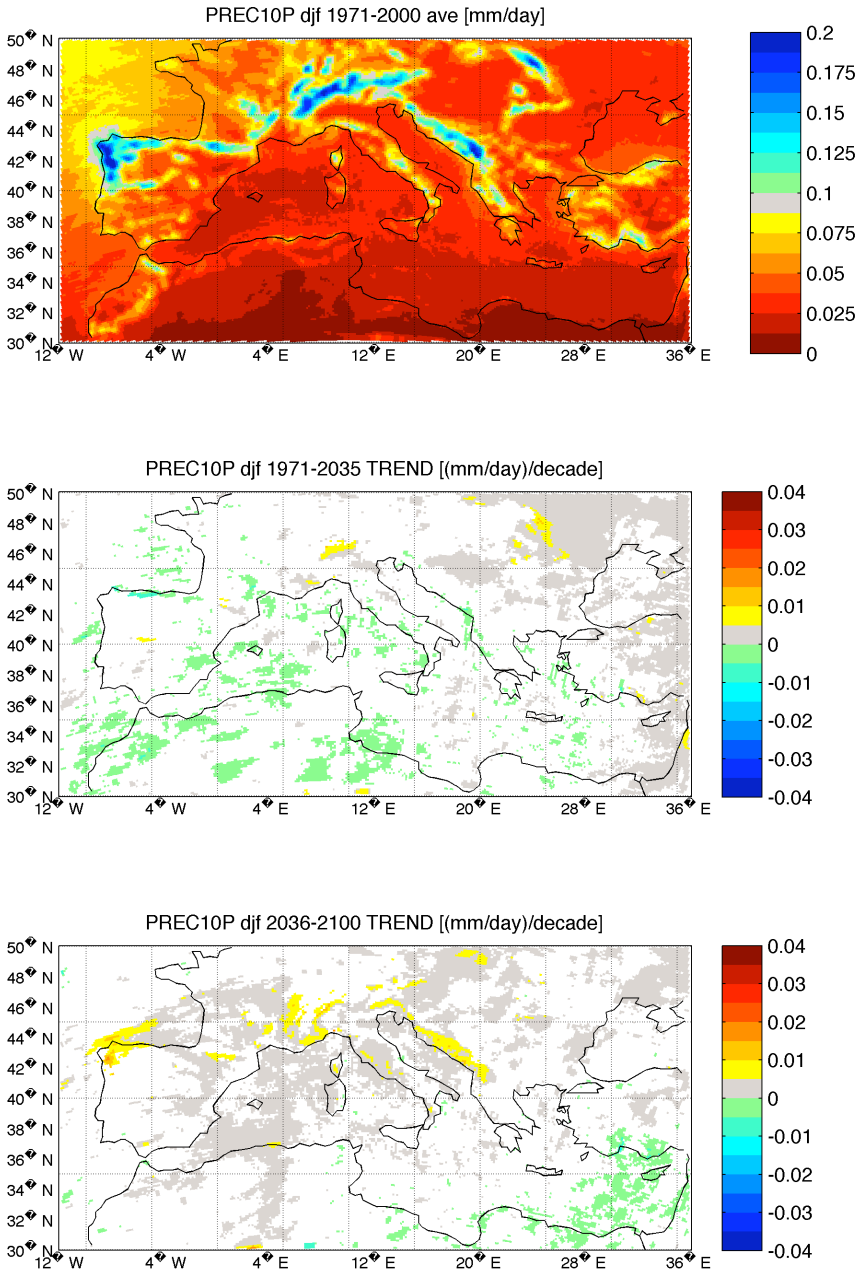

Figure 39:
PREC10P index computed for DJF season: 10^{th} percentile of the daily precipitation. The first panel shows the average of this index over the 1971-2000 considered period. The last two panes show the index linear trend during 1971-2035 and 2036-2100. White patterns identify grid points where the computed trend is not statistically significant.

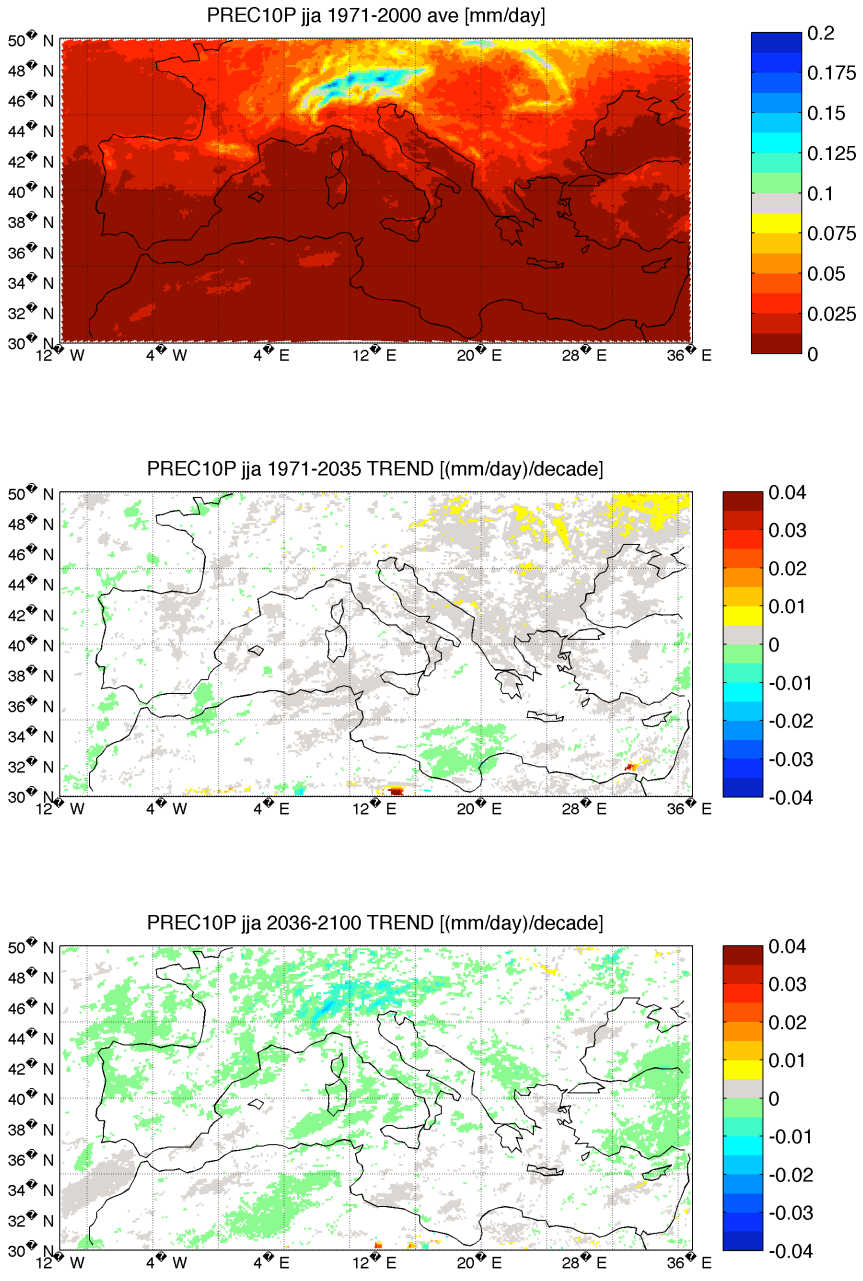

Figure 40:
PREC10P index computed for JJA season: 10^{th} percentile of the daily precipitation. The first panel shows the average of this index over the 1971-2000 considered period. The last two panes show the index linear trend during 1971-2035 and 2036-2100. White patterns identify grid points where the computed trend is not statistically significant.

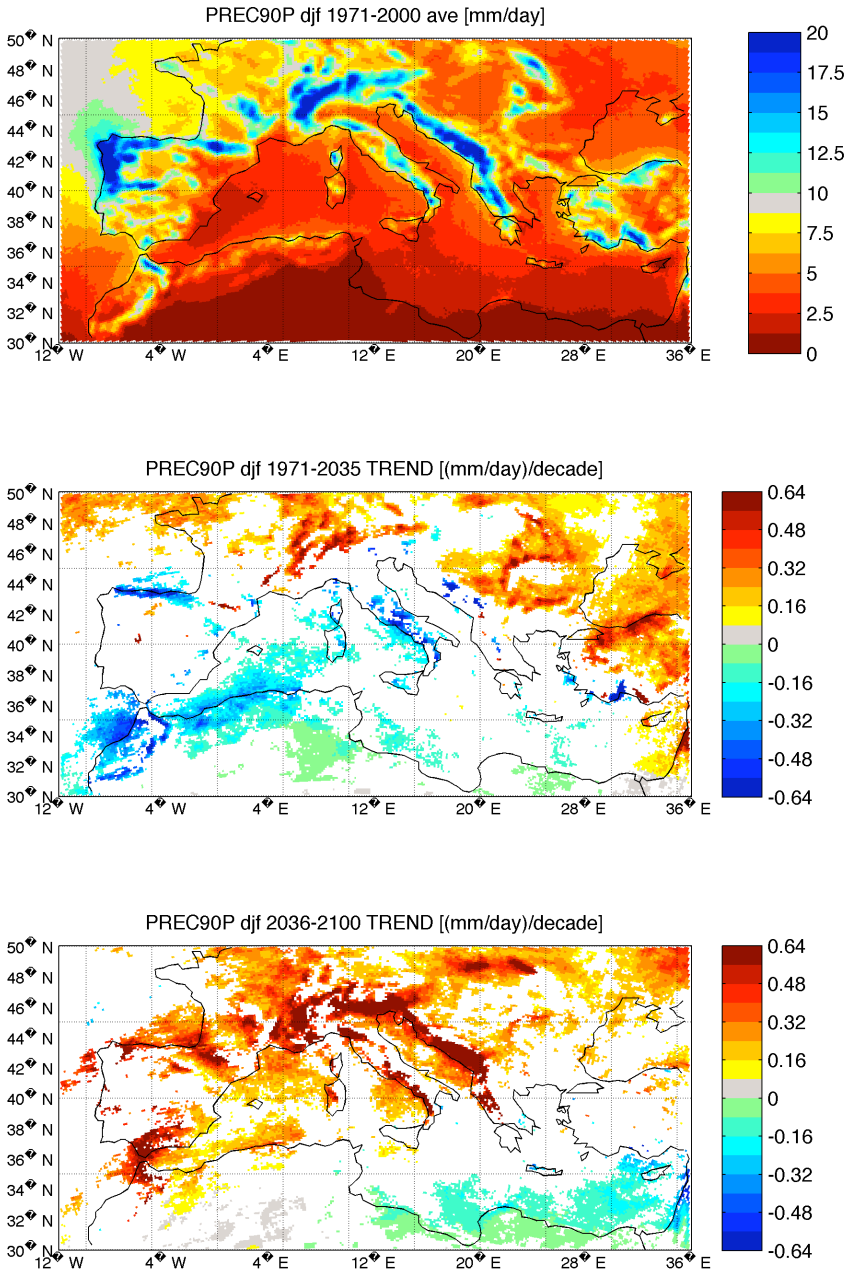

Figure 41:
PREC90P index computed for DJF season: 90^{th} percentile of the daily precipitation. The first panel shows the average of this index over the 1971-2000 considered period. The last two panes show the index linear trend during 1971-2035 and 2036-2100. White patterns identify grid points where the computed trend is not statistically significant.

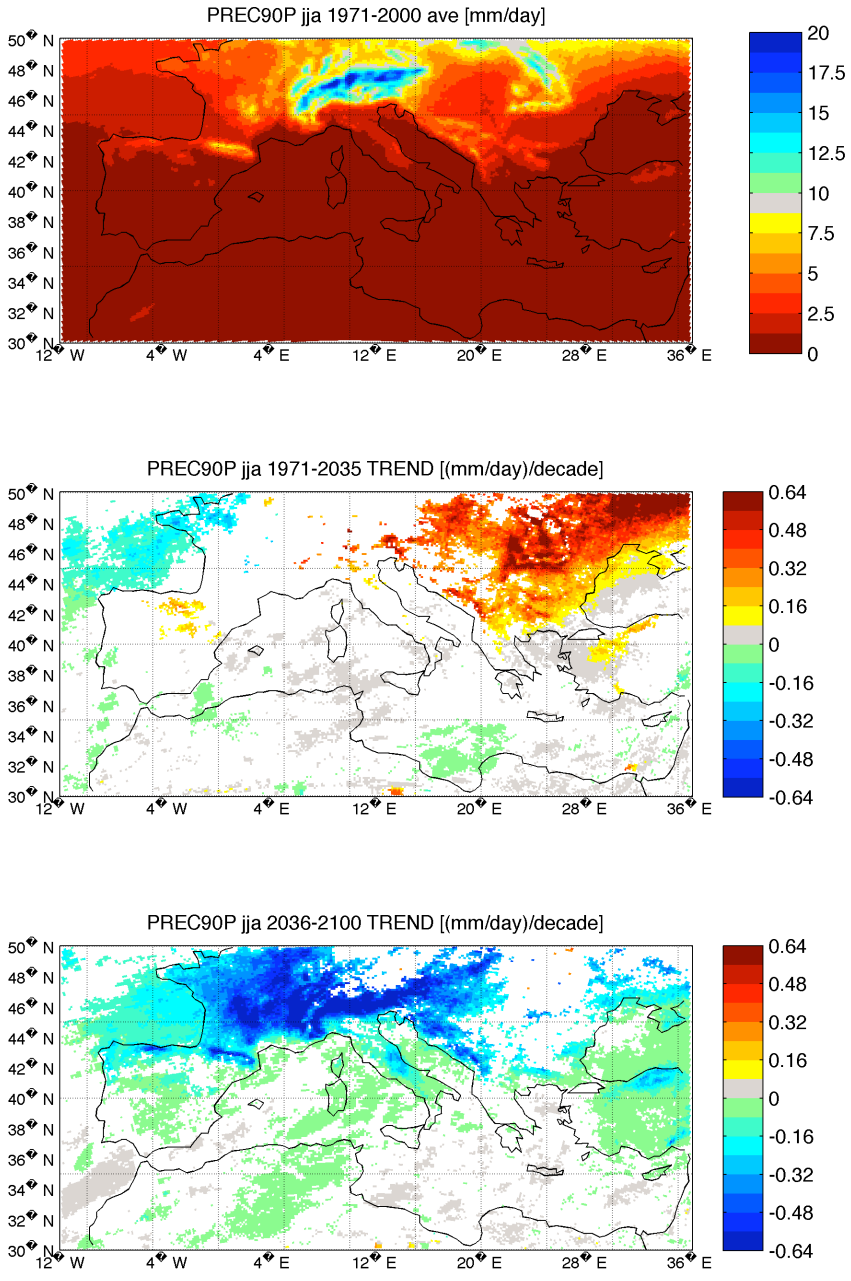

Figure 42:
PREC90P index computed for JJA season: 90^{th} percentile of the daily precipitation. The first panel shows the average of this index over the 1971-2000 considered period. The last two panes show the index linear trend during 1971-2035 and 2036-2100. White patterns identify grid points where the computed trend is not statistically significant.

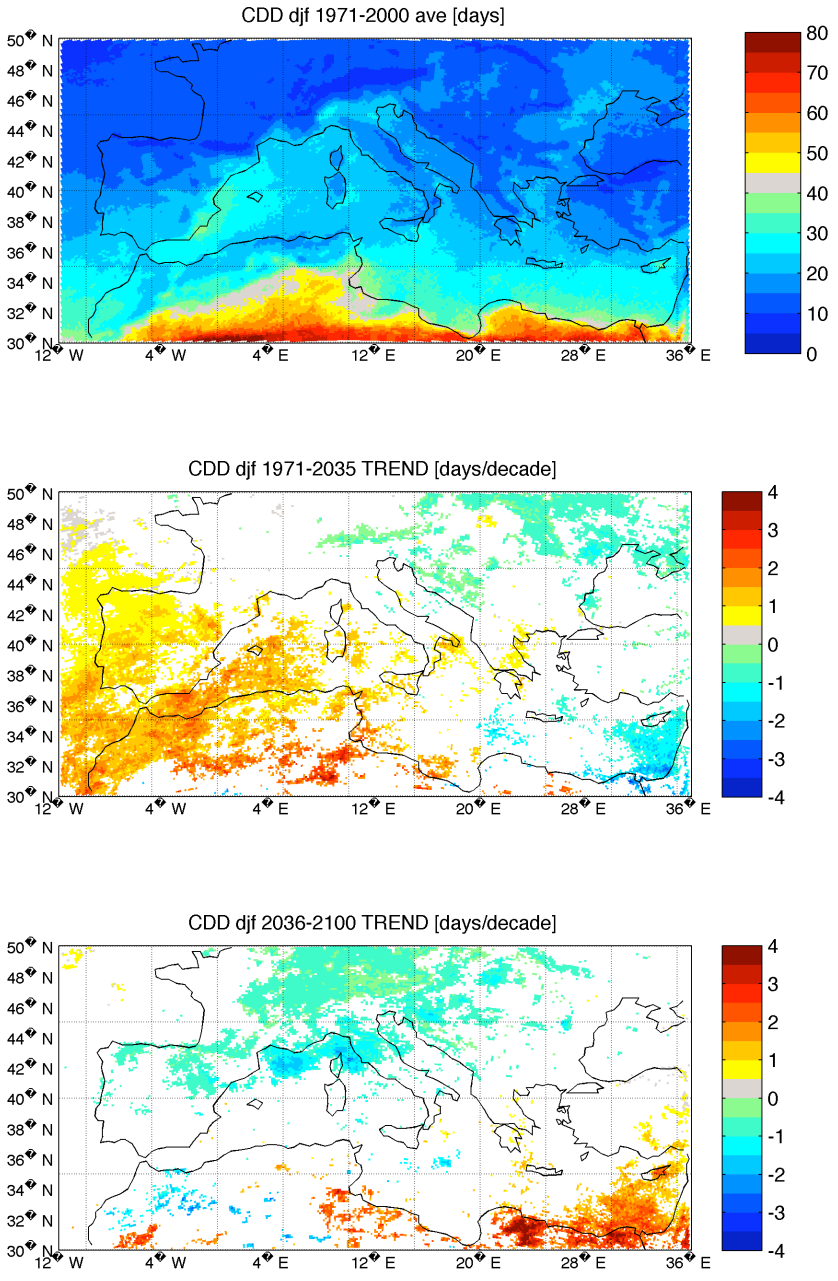

Figure 43:
CDD index computed for DJF season: Maximum number of consecutive dry days (defined as precip <= 1 mm/day). The first panel shows the average of this index over the 1971-2000 considered period. The last two panes show the index linear trend during 1971-2035 and 2036-2100. White patterns identify grid points where the computed trend is not statistically significant.

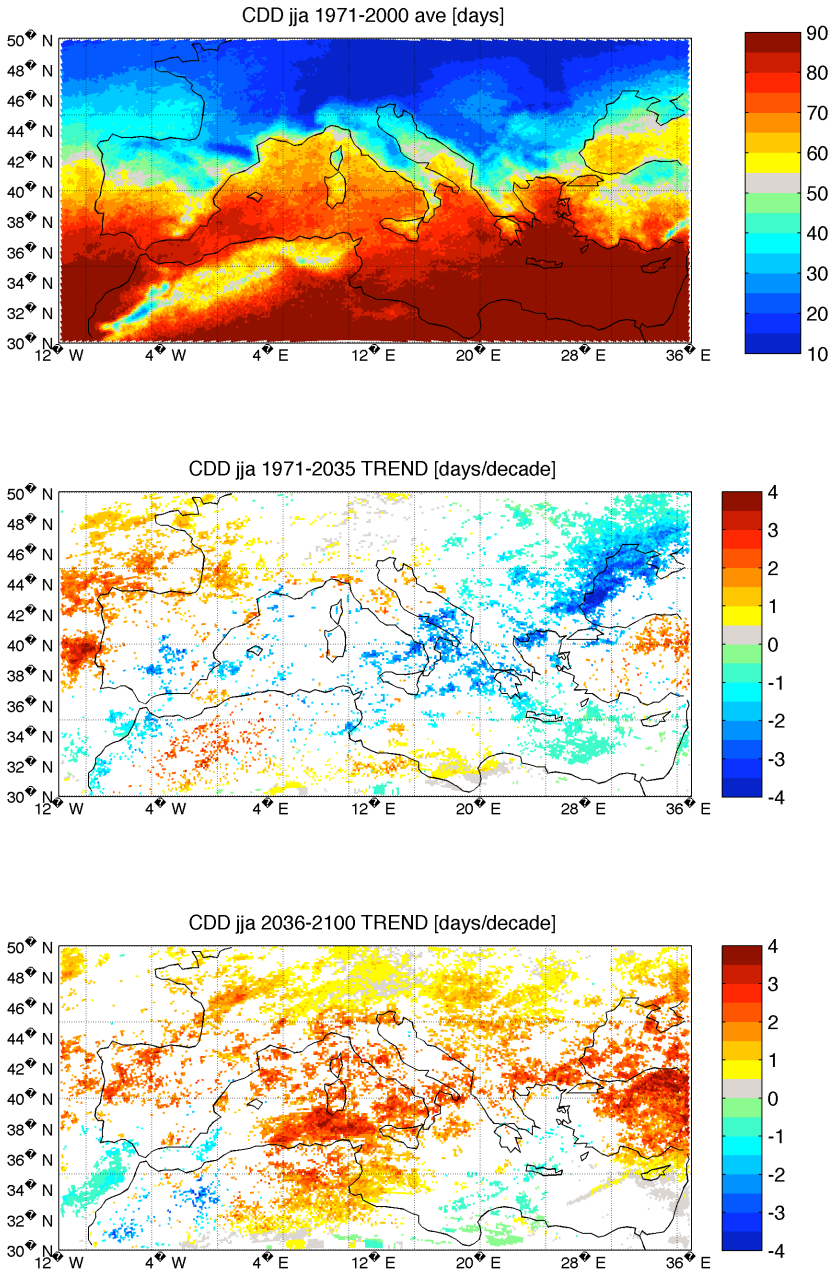

Figure 44:
CDD index computed for JJA season: Maximum number of consecutive dry days (defined as precip <= 1 mm/day). The first panel shows the average of this index over the 1971-2000 considered period. The last two panes show the index linear trend during 1971-2035 and 2036-2100. White patterns identify grid points where the computed trend is not statistically significant.

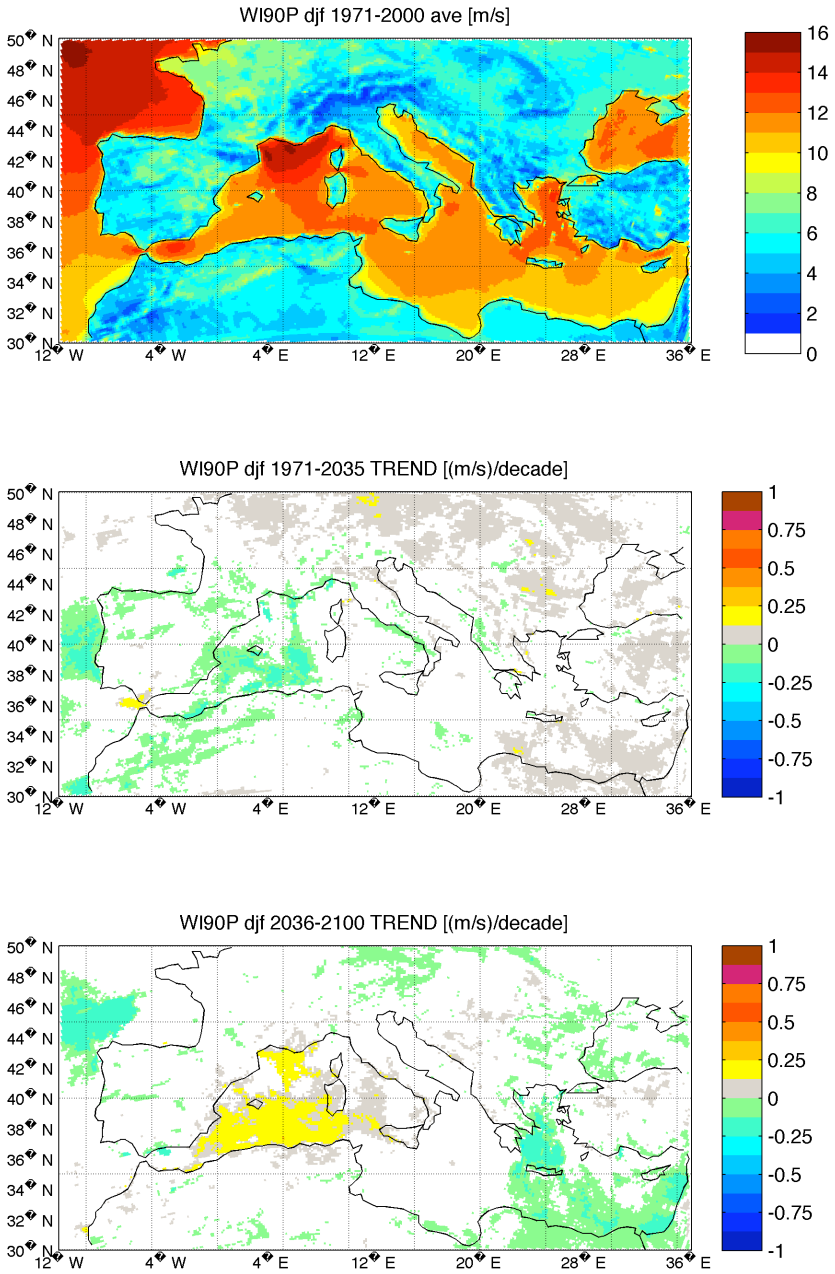

Figure 45:
WI90P index computed for DJF season: 90^{th} percentile of the 10m wind speed. The first panel shows the average of this index over the 1971-2000 considered period. The last two panels show the index linear trend during 1971-2035 and 2036-2100. White patterns identify grid points where the computed trend is not statistically significant.

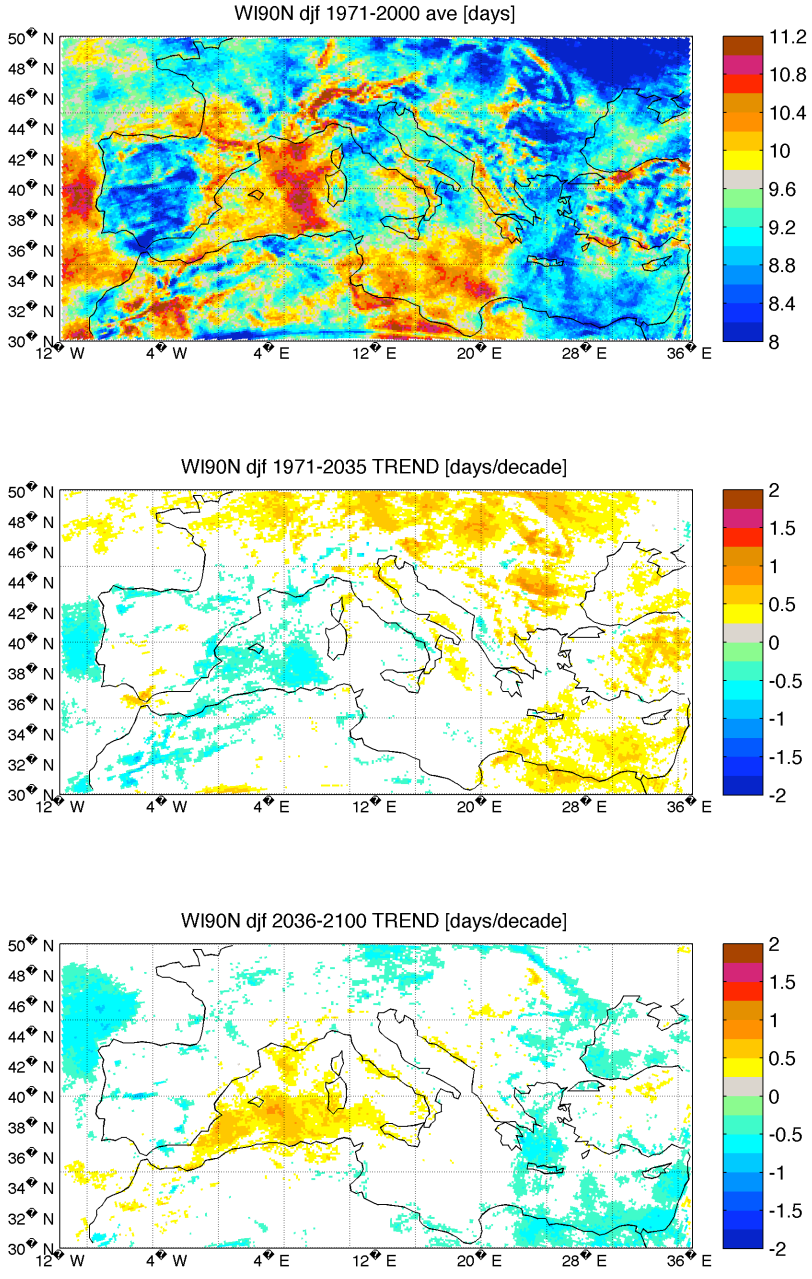

Figure 46:
WI90N index computed for DJF season: number of days with daily 10m wind speed exceeding the long term 90^{th} percentile of the 10m wind speed. The first panel shows the average of this index over the 1971-2000 considered period. The last two panes show the index linear trend during 1971-2035 and 2036-2100. White patterns identify grid points where the computed trend is not statistically significant.

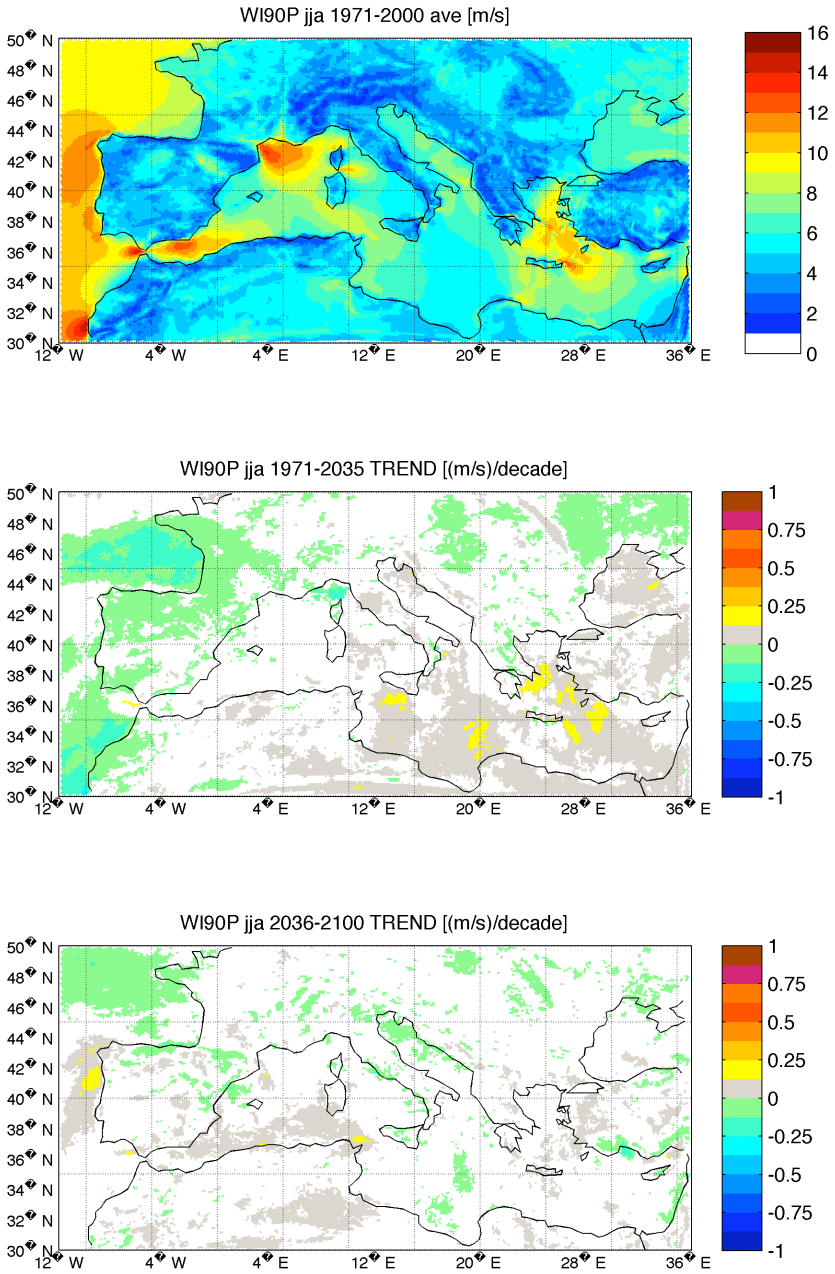

Figure 47:
WI90P index computed for JJA season: 90^{th} percentile of the 10m wind speed. The first panel shows the average of this index over the 1971-2000 considered period. The last two panes show the index linear trend during 1971-2035 and 2036-2100. White patterns identify grid points where the computed trend is not statistically significant.

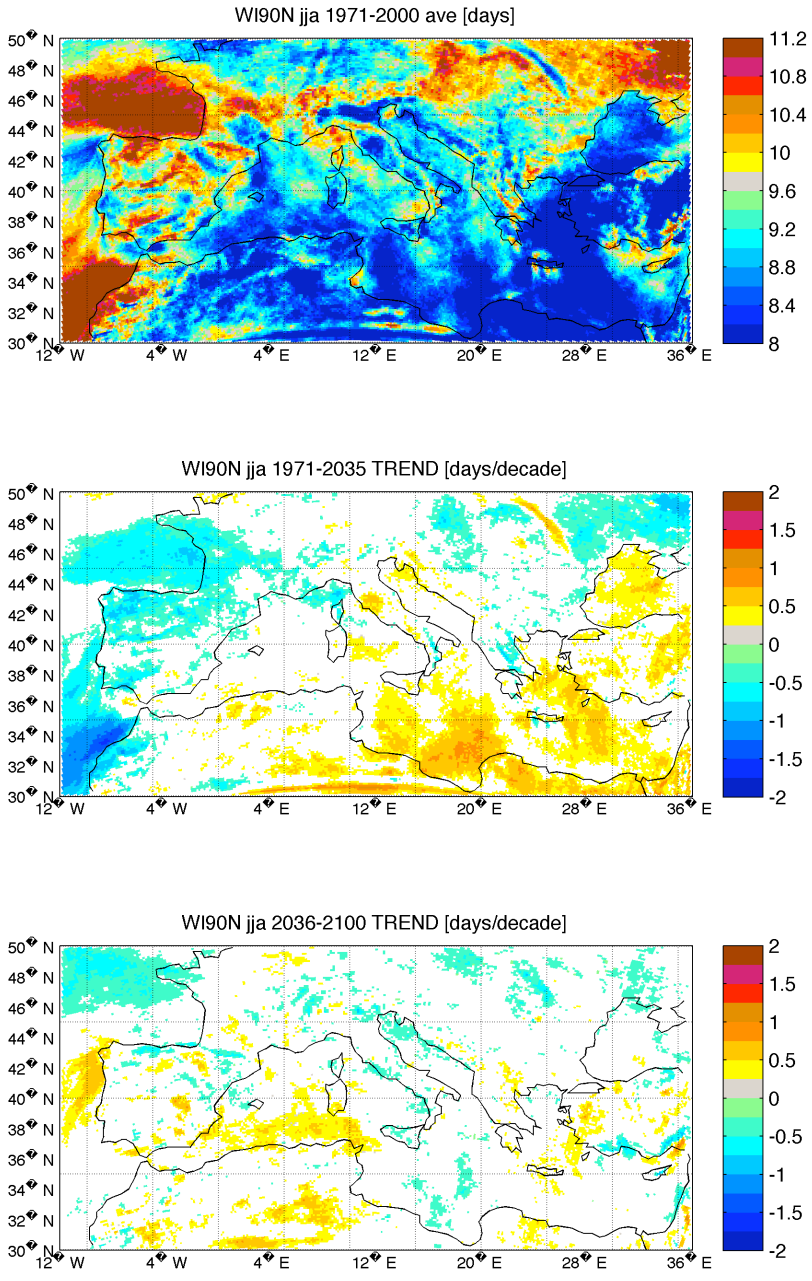

Figure 48:
WI90N index computed for JJA season: number of days with daily 10m wind speed exceeding the long term 90^{th} percentile of the 10m wind speed. The first panel shows the average of this index over the 1971-2000 considered period. The last two panes show the index linear trend during 1971-2035 and 2036-2100. White patterns identify grid points where the computed trend is not statistically significant.

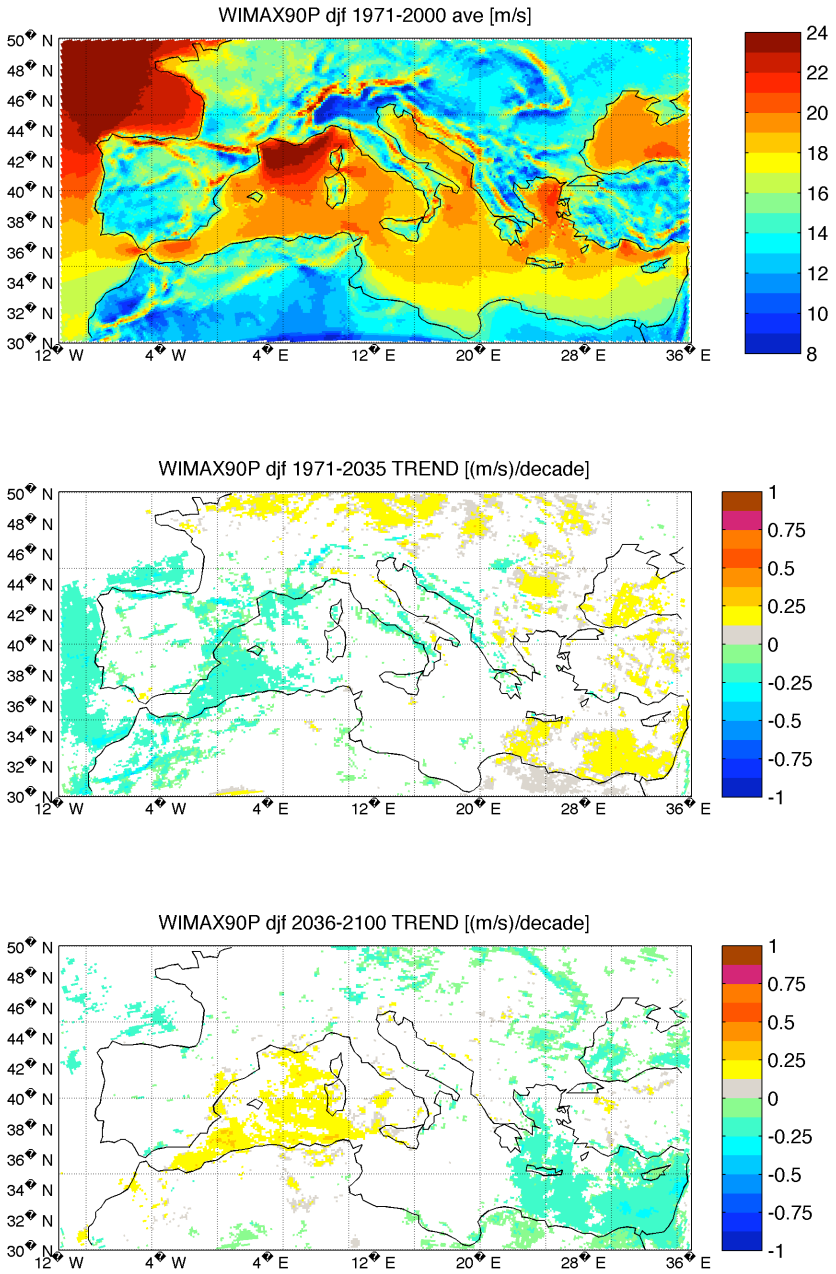

Figure 49:
WIMAX90P index computed for DJF season: 90^{th} percentile of the 10m maximum wind speed. The first panel shows the average of this index over the 1971-2000 considered period. The last two panes show the index linear trend during 1971-2035 and 2036-2100. White patterns identify grid points where the computed trend is not statistically significant.

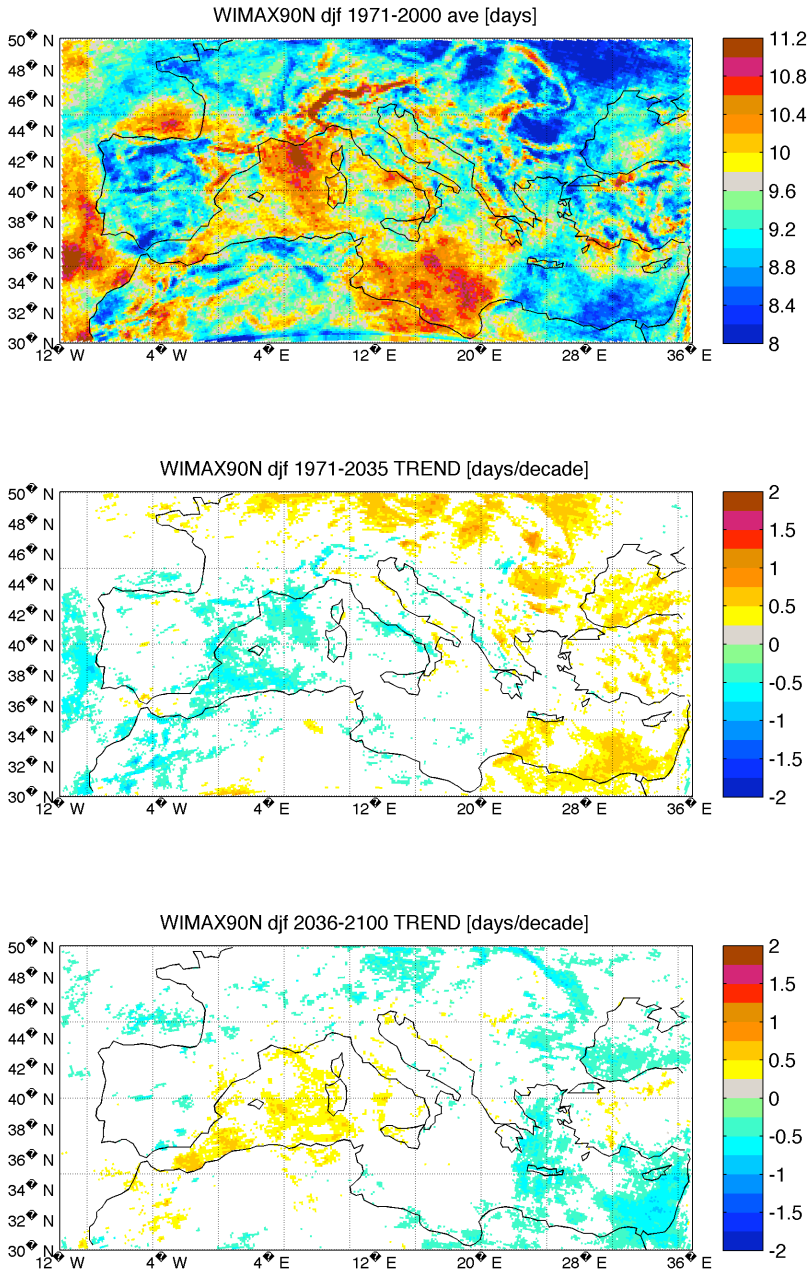

Figure 50:
WIMAX90N index computed for DJF season: number of days with daily 10m wind speed exceeding the long term 90^{th} percentile of the 10m maximum wind speed. The first panel shows the average of this index over the 1971-2000 considered period. The last two panes show the index linear trend during 1971-2035 and 2036-2100. White patterns identify grid points where the computed trend is not statistically significant.

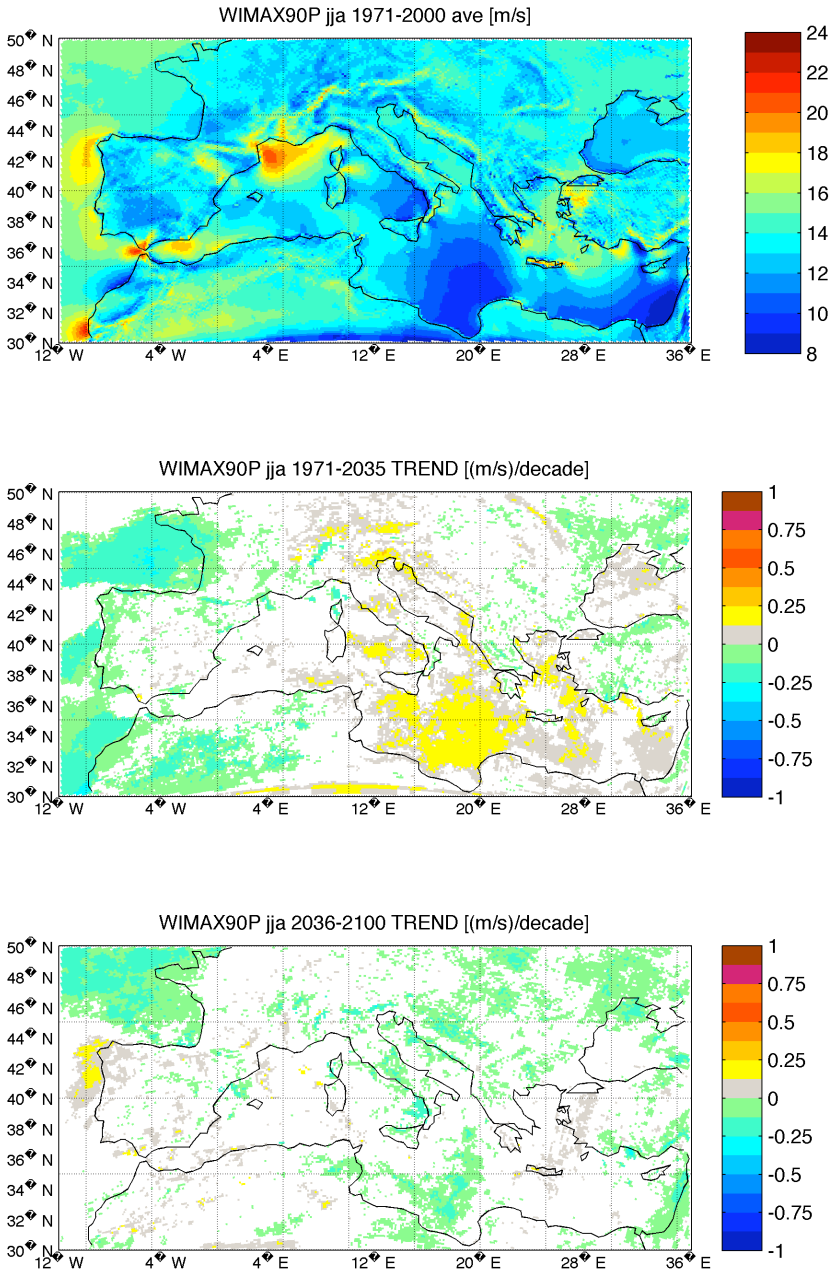

Figure 51:
WIMAX90P index computed for JJA season: 90^{th} percentile of the maximum 10m wind speed. The first panel shows the average of this index over the 1971-2000 considered period. The last two panes show the index linear trend during 1971-2035 and 2036-2100. White patterns identify grid points where the computed trend is not statistically significant.

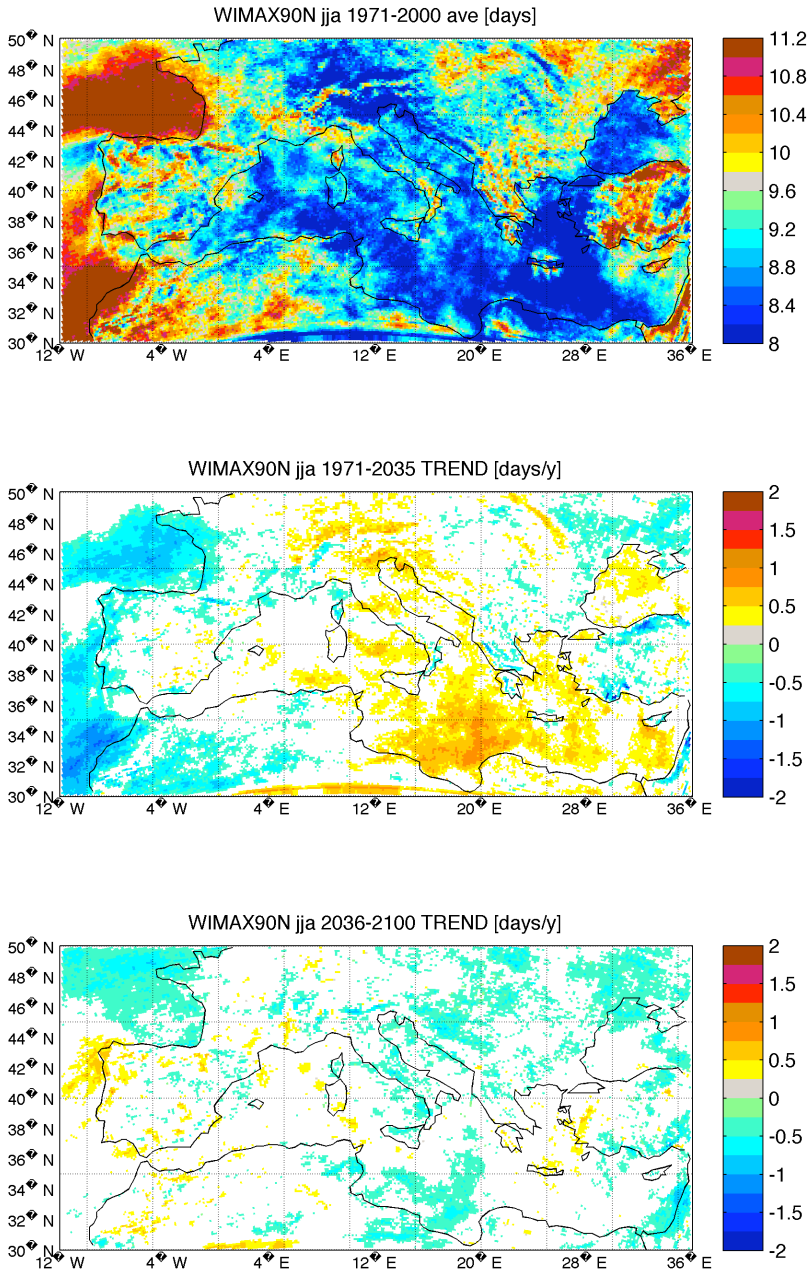

Figure 52:
WIMAX90N index computed for JJA season: number of days with daily 10m maximum wind speed exceeding the long term 90^{th} percentile of the 10m wind speed. The first panel shows the average of this index over the 1971-2000 considered period. The last two panes show the index linear trend during 1971-2035 and 2036-2100. White patterns identify grid points where the computed trend is not statistically significant.

6 Bibliography

[1] T. Beer. The interaction of wind and fire. *Boundary Layer Meteorology*, 54(3):287–308, 1990.

[2] A. Bellucci, S. Gualdi, E. Scoccimarro, and A. Navarra. NAO - ocean circulation interactions in a coupled general circulation model. *Clim. Dyn.*, 31(7-8):759–777, 2008.

[3] AF Carril, S. Gualdi, A. Cherchi, and A. Navarra. Heatwaves in europe: areas of homogeneous variability and links with the regional to large-scale atmospheric and ssts anomalies. *Clim Dyn*, 30:77–98, 2008.

[4] Roeckner E. and coauthors. The atmospheric general circulation model echam5. part i: Model description. MPI Rep. 349, MPI, 2003.

[5] P.G. Fogli, E. Manzini, M. Vichi, A. Alessandri, L. Patara, S. Gualdi, E. Scoccimarro, S. Masina, and A. Navarra. NGV-CMCC carbon (ICC): A carbon cycle earth system model. CMCC Technical Reports 61, CMCC, 2009.

[6] S. Gualdi, E. Scoccimarro, A. Bellucci, P. Oddo, A. Sanna, P.G. Fogli, M. Vichi, E. Manzini, and A. Navarra. Regional climate simulations with a global high resolution coupled model: the euro-mediterranean case. *Submitted to Clim Dyn*, 2011.

[7] S. Gualdi, E. Scoccimarro, and A. Navarra. Changes in tropical cyclone activity due to global warming: Results from a high-resolution coupled general circulation model. *J. of Clim.*, 21:5204–5228, 2008.

[8] P. Naveau, M. Nogaj, C. Ammann, P. Yiou, D. Cooley, and V. Jomelli. Statistical methods for the analysis of climate extremes. *Comptes rendus Geosciences de l'Academie des Sciences*, pages 1013–1022, 2005.

[9] P. Oddo, M. Adani N. Pinardi, C. Fratianni, M. Tonani, and D. Pettenuzzo. A nested atlantic-mediterranean sea general circulation model for operational forecasting. *Ocean Sci. Discuss.*, 6:1093–1127, 2009.

[10] B. Rockel, Will, A., and Hense A. The regional climate model cosmo-clm (cclm). *Meteorologische Zeitschrift*, 17(4):347–348, 2008.

[11] E. Scoccimarro, S. Gualdi, A. Bellucci, A. Sanna, P.G. Fogli, E. Manzini, M. Vichi, P. Oddo, and A. Navarra. Effects of tropical cyclones on ocean heat transport in a high resolution coupled general circulation model. *J. of Clim.*, 24(16):4368–4384, 2011.

[12] S. Solomon, D. Qin, M. Manning, Z. Chen, M. Marquis, K.B. Averyt, M. Tignor, and H.L. Miller. *Climate Change 2007: The Physical Science Basis. Contribution of Working Group I to the Fourth Assessment Report of the Intergovernmental Panel on Climate Change*. Cambridge University Press, Cambridge, United Kingdom and New York, NY, USA., 2007.

[13] J. Steppeler, Doms G., Schättler U., Bitzer H.W., Gassmann A., Damrath U., and Gregoric G. Meso-gamma scale forecasts using the nonhydrostatic model lm. *Meteorol. Atmos. Phys.*, 82:75–96, 2003.

[14] M. Vichi, E. Manzini, P.G. Fogli, A. Alessandri, L. Patara, S. Masina, S. Gualdi, E. Scoccimarro, and A. Navarra. Global and regional ocean carbon uptake and climate change: sensitivity to a substantial mitigation scenario. doi: 10.1007/s00382-011-1079-0, 2011.

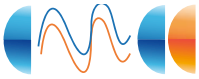

Visit **www.cmcc.it** for information on our activities and publications.

The Euro-Mediteranean Centre for Climate Change is a Ltd Company with its registered office and administration in Lecce and local units in Bologna, Venice, Capua, Sassari and Milan. The society doesn't pursue profitable ends and aims to realize and manage the Centre, its promotion, and research coordination and different scientific and applied activities in the field of climate change study.